AN ABSTRACT OF THE THESIS OF

Roger M. Samelson for the degree of Doctor of Philosophy in Oceanography presented on October 2, 1987.

Title: Observations and Modelling of Fronts and Frontogenesis in the Upper Ocean

Redacted for Privacy

Abstract approved: _____
Clayton A. Paulson

A thermistor chain was towed 1400 km through the Eastern North Pacific Subtropical Frontal Zone in January 1980. The observations resolve surface layer temperature features with horizontal wavelengths between 200 m and several hundred kilometers and vertical scales of 10 to 70 m. The dominant features have horizontal wavelengths of 10-100 km, amplitudes of 0.2 to 1.0 ^{o}C, and random orientation. Strong temperature fronts O(1-2 ^{o}C/3-10 km) are observed near 33^{o} N, 31^{o} N and 27^{o} N. There is evidence of vertically differential horizontal advection by light winds in stable conditions and vertical mixing during high winds. Temperature at 15 m depth is roughly normally distributed around the climatological surface mean. Its horizontal gradient has high kurtosis. In the band 0.1-1 cpkm, the 15 m spectrum is inversely proportional to wavenumber, consistent with predictions from

the theory of geostrophic turbulence, while the 70 m spectrum has additional variance consistent with Garrett-Munk internal wave displacements.

We formulate analytically and solve numerically a semigeostrophic model for wind-driven thermocline upwelling. The model has a variable-density entraining mixed layer and two homogeneous interior layers. All variables are uniform alongshore. A modified Ekman balance is prescribed far offshore, and the normal-to-shore velocity field responds on the scales of the local internal deformation radii, which adjust dynamically. Sustained upwelling results in a step-like horizontal profile of mixed layer density, as the layer interfaces "surface" and are advected offshore. The upwelled horizontal profile of mixed layer density scales with the initial internal deformation radii. Around the fronts, surface layer divergence occurs that is equal in magnitude to the divergence in the upwelling zone adjacent to the coast, but its depth penetration is inhibited by the stratification.

Observations and Modelling of Fronts and Frontogenesis in the Upper Ocean

by

Roger M. Samelson

A THESIS

submitted to

Oregon State University

in partial fulfillment of
the requirements for the
degree of

Doctor of Philosophy

Completed October 2, 1987

Commencement June 1988

APPROVED:

Redacted for Privacy

Professor of Oceanography in charge of major

Redacted for Privacy

Dean of College of Oceanography

Redacted for Privacy

Dean of Graduate School

Date thesis is presented October 2, 1987

Typed by researcher for Roger M. Samelson

To my parents, Hans and Nancy Samelson

ACKNOWLEDGEMENTS

I thank my advisor Clayton Paulson and the members of my committee for their support, guidance, and friendship. Clayton generously gave me the opportunity to explore a variety of projects. I owe him a debt of gratitude for his unwavering personal support. The first half of this thesis is based on his data; he guided me through its analysis. Roland de Szoeke suggested the upwelling problem that makes up the second half of this thesis, and patiently guided me through it. John Allen invited my cooperation on a separate project. Doug Caldwell supported me during my first quarter.

Rick Baumann's assistance during the analysis of the thermistor chain data went far beyond the call of duty. I am grateful to Jim Richman for conversations concerning the upwelling problem. Eric Beals and Steve Gard provided comradeship in the trenches while the bits were flying. Erika Francis, John Leland, Jeff Paduan and others kept me from going (entirely) off the deep end. Harry Beller taught me much about the musical routes to chaos. I thank the scientists and crew of the R/V Wecoma, TH 87 Leg 2, for not throwing me to the sharks when they had the motive and the opportunity. Thanks to all those over the years who have helped me to appreciate that the ocean is more than an analog device for the solution of certain partial differential equations of mathematical physics.

This research was supported by ONR under contracts N00014-87-K-0009 and N00014-84-C-0218 and by NSF under grant OCE-8541635. Computations for Chapter III were carried out on the Cray-1 at NCAR.

What in water did Bloom, waterlover, drawer of water, watercarrier returning to the range, admire?

Its universality...its vehicular ramifications in continental lakecontained streams and confluent oceanflowing rivers with their tributaries and transoceanic currents: gulfstream, north and south equatorial courses: its violence in seaquakes, waterspouts, artesian wells, eruptions, torrents, eddies, freshets, spates, groundswells, watersheds, waterpartings, geysers, cataracts, whirlpools, maelstroms, inundations, deluges, cloudbursts: its vast circumterrestrial ahorizontal curve: its secrecy in springs....

James Joyce, Ulysses

Know ye, now, Bulkington? Glimpses do ye seem to see of that mortally intolerable truth; that all deep earnest thinking is but the intrepid effort of the soul to keep the open independence of her sea...?

Herman Melville, Moby Dick

Verandahs, where the pages of the sea
are a book left open by an absent master
in the middle of another life....

Derek Walcott, Another Life

TABLE OF CONTENTS

LIST OF FIGURES

LIST OF FIGURES (continued)

LIST OF TABLES

OBSERVATIONS AND MODELLING OF FRONTS AND FRONTOGENESIS IN THE UPPER OCEAN

I. INTRODUCTION

This thesis comprises two separate projects. The common theme is fronts and frontogenesis in the upper ocean.

Fronts, regions of unusually large horizontal gradients in fluid properties, are an important form of physical oceanographic variability. Though they have received considerable attention from oceanographers (the recent monograph The Physical Nature and Structure of Oceanic Fronts (Fedorov, 1986) contains 279 references), a full understanding of their role in the ocean still awaits us.

In Chapter II, we present an analysis of upper ocean temperature data collected near the North Pacific Subtropical Frontal Zone. In this region of the North Pacific, the large-scale meridional gradients of temperature, salinity, and density are intensified in a Frontal Zone. Wind-driven convergence is the probable primary cause of this intensification (Roden, 1975). Many small scale fronts are evident in the data. Baroclinic instability is likely important in the development of these smaller scale features.

In Chapter III, we present a model for wind-driven thermocline upwelling at a coastal boundary. In this case, the action of the wind on the ocean is again frontogenetic.

Here, however, a divergence drives the frontogenesis, as fluid is drawn up at the boundary to produce horizontal gradients from vertical stratification.

The basic physics of the upwelling process analyzed in Chapter III should essentially apply (with appropriate rescaling and some additional dynamics) to wind-driven upwelling in the Subarctic gyre north of the Subtropical Frontal Zone. Since the meridional gradient in surface layer properties may be partially maintained by this upwelling, further investigations may eventually link the ideas and observations of these two Chapters in an unexpected and relatively direct manner.

II. TOWED THERMISTOR CHAIN OBSERVATIONS OF FRONTS IN THE SUBTROPICAL NORTH PACIFIC

Abstract

A thermistor chain was towed 1400 km through the Eastern North Pacific Subtropical Frontal Zone in January 1980. The observations resolve surface layer temperature features with horizontal wavelengths between 200 m and several hundred kilometers and vertical scales of 10 to 70 m. The dominant features have horizontal wavelengths of 10-100 km, amplitudes of 0.2 to 1.0 ^{o}C, and random orientation. Associated with them is a plateau below 0.1 cpkm in the horizontal temperature gradient spectrum that is coherent between 15 and 70 m depths. They likely arise from baroclinic instability. Strong temperature fronts O(1-2 ^{o}C/3-10 km) are observed near 33^{o} N, 31^{o} N and 27^{o} N. Temperature variability is partially density compensated by salinity, with the fraction of compensation increasing northward. There is evidence of vertically differential horizontal advection by light winds in stable conditions, vertical mixing during high winds, and shallow convection caused by wind-driven advection of denser water over less dense water. Temperature at 15 m depth is roughly normally distributed around the climatological surface mean, with a standard deviation of approximately 0.7 ^{o}C, while its horizontal gradient has high kurtosis and

maximum values in excess of 0.25 ^{o}C/100 m. In the band 0.1-1 cpkm, the 15 m spectrum is very nearly inversely proportional to wavenumber, consistent with predictions from geostrophic turbulence theory, while the spectrum at 70 m depth has additional variance that is consistent with Garrett-Munk internal wave displacements.

II.1 Introduction

The North Pacific Subtropical Frontal Zone is a band of relatively large mean meridional upper ocean temperature and salinity gradient centered near 30^{o} N (Roden, 1973). Its existence is generally attributed to wind-driven surface convergence and large-scale variations in air-sea heat and water fluxes (Roden, 1975). A recent attempt has been made to determine the associated large-scale geostrophic flow (Niiler and Reynolds, 1984), and hydrographic surveys (Roden, 1981) of the Subtropical Frontal Zone have revealed energetic mesoscale eddy fields. However, little is known about the dynamics of the local mesoscale circulation or the detailed structure, generation, and dissipation of individual frontal features.

Here we report on an investigation of the upper ocean thermal structure of fronts in the North Pacific Subtropical Frontal Zone. We use the term "Frontal Zone" rather than "Front" because these wintertime measurements show randomly

oriented multiple surface fronts up to 2 ^{o}C in magnitude and less than 10 km in width. Observations were made in January 1980 with a towed thermistor chain that measured temperature at 12 to 21 depths in the upper 100 m of the water column. The thermistor chain was towed a distance of 1400 km in an area of the Pacific bounded by 26^{o} and 34^{o} N, 150^{o} and 158^{o} W. The observations resolve surface layer temperature features with horizontal wavelengths between 200 m and several hundred km and vertical scales of 10 to 70 m. The towed thermistor chain and data collection procedure are described in Section II.2. Section II.3 is devoted to a description of the fronts, their magnitude and horizontal scales, temperature-salinity compensation, vertical stratification, and response to wind. Probability densities of surface (15 m) temperature (with the climatological mean removed) and surface temperature gradient are presented in Section II.4.a. Horizontal wavenumber spectra of temperature and temperature gradient at several depths between 15 and 70 m are presented in Section II.4.b. In Section II.5, the high wavenumber tail of the temperature spectrum is compared with the predictions of the theory of geostrophic turbulence (Charney, 1971). Section II.6 contains a summary.

II.2 Instrumentation and data collection

The thermistor chain tows were made during FRONTS 80, a multi-investigator endeavor focused on the Subtropical Frontal Zone near 31° N, 155° W, in January 1980. Other measurements by other investigators included CTD surveys (Roden, 1981), remotely sensed infrared radiation (Van Woert, 1982), XCP velocity profiles (Kunze and Sanford, 1984), and drifting buoy tracks (Niiler and Reynolds, 1984).

The thermistor chain has been described in Paulson et al. (1980). The chain was 120 m long, with a 450 kg lead depressor to maintain a near vertical alignment while it was towed behind the ship. Sensors were located at approximately 4 m intervals over the lower 82 m. These sensors included 27 Thermometrics P-85 thermistors and three pressure transducers. The thermistors have a response time of 0.1 s, relative accuracy of better than 10^{-3} °C, and absolute accuracy of roughly 10^{-2} °C. Data were recorded at a sampling frequency of 10 Hz. For this analysis, individual thermistor data records were averaged to values at 100 m intervals using ship speed from two-hourly positions interpolated from satellite fixes. Since this speed varied (from 2 to 6 m s^{-1}), the averaged values contain a variable number of data points (from 166 to 502). The averaging removes the effects of ship roll and pitch and surface

gravity waves. A maximum of 21 and a minimum of 12 thermistors functioned for entire tows. Thermistor depths were obtained from the ship's log speed and a model of the towed chain configuration calibrated by data from the pressure transducers. Temperature measurements were obtained at maximum and minimum depths of 95 m and 4 m.

The tow tracks are displayed in Figure II.1. The four tows are labeled by number in chronological order. Since the tracks for Tows 2 and 3 overlap, the track for Tow 3, which took place on 25 January, is displayed separately, overlaid on a contour of temperature at 20 m from the Roden CTD survey during 24-30 January. Tows 2 and 3 are each divided into sections, labeled a and b, by course changes. The tow start and finish positions and times are given in Table II.1. During 19-26 January, the ship remained within the rectangle indicated by dashed lines in Figure II.1.

Surface salinity was determined from temperature and conductivity measured by a Bisset Berman CTD located in the ship's wet lab, to which water was pumped from a sea chest at approximately 5 m depth. The cycle time for the fluid in this system was roughly 5-10 minutes during most of the experiment. The CTD temperature, corrected for (approximately 1 ^{o}C) intake warming by comparison with data from the uppermost thermistor, was used to obtain surface density. CTD conductivity and temperature were recorded

hourly (once every 10-20 km at typical tow speeds), as were surface wind speed and direction (from an anemometer at 34.4 m height), dry and wet bulb air temperatures, and incident solar radiation.

II.3 Observations

Sea surface temperature and salinity from ship-board CTD measurements during 16-28 January are displayed with contours of σ_t (density) in Figure II.2. The data range over 7 ^{o}C in temperature (T) and 1 ppt in salinity (S). Though temperature may vary by 1 ^{o}C at constant salinity, most of the data approximately obey a single identifiable T-S relation, with the exception of four points with T > 20.5 ^{o}C, S $\tilde{=}$ 35.1 ppt, which occurred after the encounter of a strong front at the southern end of Tow 4. Salinity tends to compensate temperature, so the density variations are small, but relative temperature still tends to indicate relative density (warmer, more saline, water is typically less dense).

Surface temperature, salinity, and σ_t are displayed versus latitude in Figure II.3. Scales have been chosen using the equation of state so that a unit distance change in temperature (salinity) at constant salinity (temperature) corresponds approximately to a unit distance change in σ_t. Temperature and salinity tend to decrease toward higher latitudes. The corresponding density gradient is relatively

small, since the large-scale temperature and salinity gradients are density-compensating. Features with smaller horizontal scales also show compensation. A front near 30° N was crossed several times during 19-27 January and appears as a noisy step-like, partially compensated, feature. (Its apparent sharpness is exaggerated by a set of measurements taken during frontal transects at constant latitude.) The large temperature feature near 33° N is roughly 70% compensated by salinity. In contrast, the 2 °C front near 27° N has negligible salinity variation. There appears to be a density feature with roughly 300 km wavelength between 31° N and 34° N.

For each of the tows, Figure II.4 displays traces of 500 m horizontal averages of nominal 15 m (solid line) and 70 m (dashed line) thermistor temperature. These are respectively the shallowest and deepest depths at which thermistor measurements were made during all four tows. The dominant temperature features have horizontal wavelengths of 10 to 100 km, amplitudes of 0.2 to 1.0 °C, and no apparent preferred orientation with respect to the large-scale (climatological) temperature gradient. Satellite imagery of the Subtropical Frontal Zone in January and February 1980 (Van Woert, 1981, 1982), some of which is precisely simultaneous with the tows, shows a sea surface temperature field composed of highly distorted isotherms, such as result from advection of a

tracer by a strain field, rather than a collection of isolated patches of random temperature. The thermistor chain tows are cross-sections of this field. On horizontal scales of hundreds of kilometers, several large fronts, across which the temperature change (roughly 1 ^{o}C or more) has the same sign as the large-scale gradient, give a step-like appearance to the temperature record.

The salinity-compensated temperature structure that dominates Tow 1 is visible near 33^{o} N in Figure II.3. Measured horizontal temperature gradients exceeded 0.25 ^{o}C/100m in the front near 110 km, the largest observed during the experiment.

In Tow 2a, a large front was encountered at 200 km, near 30^{o} N. The feature in Tow 2b near 70 km appears to be a meander of the same front. This meander is visible in infrared satellite imagery from 17 January 1980 (Figure 2a, Van Woert, 1982).

Tow 3, made on 25 January, was contained in the region covered by a CTD survey (Roden, 1981) during 24-31 January. The tow is roughly perpendicular to the isotherms of the surveyed front (Figure II.1b). The mean temperature gradient is large over this entire tow. The sharp frontal boundary near 18 ^{o}C observed a week earlier at the same location during Tow 2a, does not appear in Tow 3. A tongue of warm water was crossed at the southern end of the tow, with a

front at about 18.5 ^{o}C. There is frontal structure near 60 km, at about 17.5 ^{o}C, in both Tows 3a and 3b. Note the similarity of Tows 3a and 3b, which were made on the same track (in opposing directions) but several hours apart.

The largest temperature front encountered during the experiment, with horizontal gradient reaching 1.5 ^{o}C/3 km and a temperature change of roughly 2 ^{o}C over 10 km, occurred near 27^{o} N at 350 km in Tow 4. The salinity change across this feature is small and in fact enhances the density change, which is approximately 0.5 kg m^{-3} over 10 km, most of it occurring over 3 km. This is larger than the density variability observed over the entire remainder of the experiment. Isotherm cross-sections of this front are shown in Figure II.5a. The geostrophic vertical shear across the front is roughly 10^{-2} s^{-1} at the surface. Large amplitude internal wave vertical displacements of the seasonal thermocline are visible.

The vertical temperature gradient between 15 m and 70 m was generally weak except in regions near frontal features. During Tow 1, appreciable vertical gradients appear only within 10-15 km of the fronts. During Tow 2, some vertical gradients occur up to 25-30 km from fronts (though there may be closer fronts that lie off the tow track). The upper 70 m are nearly homogeneous in temperature over most of Tow 3a. A small amount of stratification is evident near features

between 50 and 75 km and in the warm tongue near 110 km. These features and the associated vertical gradients are evident as well in Tow 3b, which followed the same track on the opposite course. In Tow 4, as in Tows 1 and 2, vertical gradients are found consistently near frontal features.

Often the upper sections of individual fronts appear displaced horizontally by several kilometers from the lower sections. During Tow 2, particularly over the interval 125-300 km, 15 m temperatures have traces that are similar to the 70 m temperatures but offset to the north. Winds (Table II.2) during 17 January were from the south, and may have displaced a shallow layer northward and eastward. Isotherm cross-sections of the feature near 135 km are shown in Figure II.5b. (Note that the presence of a temperature inversion implies an anomalous local T-S relation, according to which the warmer, more saline water is denser.) The displacement can only be estimated, since the angle of incidence of the tow track across the front is unknown, but it appears to be a few kilometers. This is an appropriate value for Ekman layer flow in response to light winds whose direction varies on a 2-5 day time scale, and is typical of such features in the data, most of which occurred after periods of light winds. Estimates of daily average buoyancy flux, made from hourly bulk estimates of surface fluxes, are shown in Table 2, and Monin-Obukhov depths calculated from the flux estimates are

given in the stable cases (downward buoyancy flux). The uncertainty in the flux estimates is roughly 20%. The Monin-Obukhov depth for 17 January, the date of the observations shown in Figure II.5b, is 62 m. This is comparable to the depth of the displaced upper section. Convection in the mixed layer may have prevented a similar structure from forming as wind stress forced denser fluid over less dense fluid at the right-hand front in Figure 5b.

Vertical gradients in the surface layer are negligible over the last 70 km of Tow 2 in spite of horizontal gradients as large as those over the first 540 km. During this last period of Tow 2b, local wind speeds rose from 5-10 m s^{-1} to 20 m s^{-1}, where they remained until after the tow was terminated. (Table II.2 gives daily vector averaged hourly winds; daily average magnitudes are larger.) The surface layer is nearly uniform in temperature to 70 m depth over most of Tow 3 as well. Maximum wind speeds of 20 m s^{-1} were attained in this region two days prior to Tow 3. The absence of vertical gradients during these two periods is likely due to vertical mixing in response to the high winds. Tow 3 was taken along part of the line covered by Tow 2a and runs between the locations of hydrographic stations occupied by the CTD survey (Roden, 1981). The surface temperature in this region decreased by approximately 1 ^{o}C between Tows 2a and 3. Roden (1981) interprets this decrease as southward

advection of a tongue of cold water in a frontal meander, but cooling by entrainment may also have contributed. Large et al. (1986) present evidence for large entrainment events in the North Pacific during the fall season. These appear to be shear mixing events driven by the near-inertial response to storms.

A 0.7 ^{o}C temperature inversion, roughly 5 km wide, occurred at 100 km, near the well-compensated front encountered during Tow 1. Isotherm cross-sections of this feature are displayed in Figure II.5c. The presence of an inversion implies an anomalous local T-S relation, according to which the warmer, more saline water is denser. The warm, dense water most likely originated from the warm side of the front, with which it may be contiguous. The wind record (Table II.2) suggests an Ekman flow to the southeast, nearly normal to the tow track, so that the cooler surface water may have been advected over the warmer water from the northwest.

II.4 Analysis

II.4.a Statistics

To characterize the temperature variability statistically, we have calculated probability densities of temperature gradient and temperature deviation from climatology. Table II.3 lists climatological surface

temperatures for January and February from 100 years of ship observations and 27 years of hydrocasts (Robinson, 1976). Figure II.6 shows the probability density of the deviation of 15 m temperatures from a fit, linear in latitude in the intervals 25-30° N and 30-35° N, to the January climatology. As noted by Roden (1981), the surface layer temperatures are colder on average than the climatological means. The apparent bimodality is probably due to poor statistics. The standard deviation is roughly 0.5 °C. Relative to the climatological gradient, this would correspond to an adiabatic meridional displacement of 80-100 km. From drifters deployed near 30° N, 150° W, Niiler and Reynolds (1984) compute a mean northward surface velocity of 1-2 cm s^{-1} during 27 January through 30 April 1980. From infrared imagery, Van Woert (1982) estimates an e-folding time of 60 days for a large frontal meander near 30 N during January and February 1980. The meridional displacement scale is comparable to the product of these velocity and time scales. Standard mixing-length arguments yield an eddy diffusivity (as velocity times length or length squared divided by time) of 1-2 x 10^3 m^2 s^{-1}. This is an order of magnitude smaller than typical values used in numerical models (e.g., Lativ, 1987).

Horizontal 100 m mean temperature gradients were calculated from differences of adjacent 15 m temperatures.

Figure II.7 displays the probability density of these gradients. The dotted line represents a Gaussian distribution with the observed mean and standard deviation. The observed kurtosis is 76, much larger than the Gaussian value of 3. This suggests the presence of a velocity field that strains the temperature gradients to small scales. The large kurtosis is characteristic of processes with sharp transitions between small and large values. It measures the front-like nature of the surface temperature field, which is dominated by intermittent large gradients separated by regions of small gradients. Qualitatively similar distributions of temperature and velocity gradients occur at small scales in three-dimensional turbulence (Monin and Yaglom, 1975). Calculations of the kurtosis for distributions of average horizontal gradient over distances from 100 m to 100 km show that the kurtosis increases sharply below scales of 10 km, with an evident but irregular change in dependence at a few hundred meters, roughly the vertical scales of the surface boundary layer.

II.4.b Spectra

Figure II.8 displays the ensemble averaged horizontal wavenumber spectrum of 15 m horizontal temperature gradient, band averaged to 5 bands per decade. The variability between 10 and 100 km wavelengths that is evident in the time series

dominates the spectrum. At these wavenumbers and at wavenumbers above 1 cpkm, the spectrum is approximately constant. Between 0.1 cpkm and 1 cpkm, the spectrum is very nearly proportional to k^{-1}, where k is wavenumber.

We associate the low wavenumber plateau with the mesoscale eddy field, the likely source of the dominant temperature features. The constant spectral level is a typical signature of an eddy production range, which may be driven by baroclinic instability. This instability generally prefers the scale of the internal deformation radius. The first local internal deformation radius, calculated using a FRONTS 80 CTD station for the upper 1500 m supplemented by deep data from a 1984 meridional transect, is 40 km, which lies within the energetic plateau, toward its less resolved low wavenumber end. The break in slope at the high wavenumber end of the plateau occurs near 0.1 cpkm, at roughly the fifth internal deformation radius. The constant spectral level at wavenumbers above 1 cpkm is likely due to temperature gradient production in the surface boundary layer.

Figure II.9 displays horizontal wavenumber spectra of 15 m horizontal temperature gradient from each individual tow, band averaged to 10 bands per decade. The spectral levels vary by roughly half a decade. The spectral shapes are nearly uniform, despite the apparent difference in the

qualitative nature of the records noted in Section II.3 (e.g., the single large feature in Tow 1 versus the myriad smaller features in Tows 2a, 2b). Each spectrum has a broad peak or plateau at low wavenumber, a break in slope near 10 km, and is approximately proportional to k^{-1} between 10 km and 1 km. A minimum occurs between 1 km and 350 m wavelengths in three of the five spectra. A secondary peak appears near 350 m in these three spectra, followed by a decrease toward the Nyquist wavelength (200 m). The spectra appear to fall off slightly toward wavelengths larger than 50 km. In this region however the number of data points is small and the 95% confidence intervals large. The spectrum from Tow 3b is not shown. At the 95% confidence level, it is essentially indistinguishable from the Tow 3a spectrum. Because of the close time and space scales, we interpret this as a lack of independence between the two spectral estimates from Tow 3, and have only included the estimate from Tow 3a in the ensemble average.

Figure II.10 displays ensemble averaged horizontal wavenumber spectra of 15 m and 70 m temperature, band averaged to 5 bands per decade. We interpret the difference between the spectral levels at 15 m and 70 m in the bands above 0.1 cpkm as internal wave vertical displacements at 70 m. Since the average vertical temperature gradients are small at 15 m (less than 10^{-4} ^{o}C m^{-1}; at 70 m they are

typically 10^{-2}-10^{-3} $^{o}C\ m^{-1}$), and since the vertical internal wave velocities must vanish at the surface, temperature variance from internal wave isotherm displacements will be small at 15 m. If the 70 m spectrum is composed of the sum of an internal wave vertical displacement spectrum that is uncorrelated with the 15 m spectrum and a spectrum (due to other processes) equal in variance to the 15 m spectrum at each wavenumber, the 70 m internal wave spectrum will be the difference of the power spectra at 70 m and 15 m. (Differencing the series leads to an overestimate of the internal wave variance, as incoherent parts not due to internal waves will contribute to the power spectrum of the differenced series.) Using average vertical temperature gradients at 70 m from entire tow means of surrounding thermistors to estimate displacements and the local buoyancy frequency, we obtain for Tows 2 and 4 the internal wave energy spectral estimates shown in Figure II.11. The empirical Garrett-Munk prediction (Eq. A12, Katz and Briscoe, 1979; Garrett and Munk, 1972), with Desaubies (1976) parameters $r = 320\ m^2\ h^{-1}$ and $t = 4 \times 10^{-4}$ cph cpm^{-1}, is plotted for comparison. The spectral levels are mostly within 2 to 3 times the predicted values, and the spectral slopes show excellent agreement. A large temperature inversion and small vertical gradients prevented reliable calculations for Tows 1 and 3. Even in Tows 2 and 4, average

temperature differences of surrounding thermistors are not far from the noise level of the calibrations, so these estimates have limited value as measurements of internal wave energy. They are however consistent with the assumption that the difference in the 70 m and 15 m spectral levels in the 0.1-1 cpkm band is due to internal waves, and that the variance in the 15 m spectrum in this band is due to other processes. Below 0.1 cpkm, where the break in slope in the 15 m spectrum occurs, the internal wave energy appears to fall off. This apparently fortuitous correspondence gives the 70 m spectrum a nearly uniform slope (Figure II.10).

Figure II.12 displays ensemble averaged spectra of horizontal temperature gradients at 15, 23, 31, 50, and 70 m, as well as ensemble averaged coherence from cross-spectra between the 15 m record and the others, all band averaged to 5 bands per decade. There is significant vertical coherence in the 0.1-1 cpkm band over most of the surface layer. Where the internal wave variance raises the spectral levels above the 15 m values, coherence is rapidly destroyed. This occurs at successively shorter wavelengths as the vertical separation decreases, presumably since only short wavelength internal waves may exist on infrequent shallow patches of vertical gradient.

II.5 Geostrophic turbulence

We have interpreted the low wavenumber plateau in the 15 m horizontal temperature gradient spectrum (Figure II.8) as the signature of the mesoscale eddy field and a probable baroclinic production range, and the high wavenumber plateau as a surface boundary layer production range. At wavenumbers above 0.1 cpkm, internal waves consistently account for the difference between the 70 m and 15 m spectra (Figures II.10 and II.11). It remains to identify the source of the additional temperature variance in the 0.1-1 cpkm wavenumber band. In this band, the temperature gradient spectrum has 95%-significant vertical coherence and is very nearly proportional to k^{-1} (Figures II.8 and II.9). Charney (1971) predicted a k^{-3} subrange in the potential energy spectrum above a baroclinic production range. If the potential energy spectrum has the same slope as the temperature spectrum in the 0.1-1 cpkm band, the observations will be consistent with this prediction, since the temperature spectrum (Figure II.10) is proportional to k^{-2} times the temperature gradient spectrum.

Charney (1971) discovered a formal analogy that holds under certain conditions between the spectral energy evolution equations associated with the two-dimensional Navier-Stokes equations and the quasigeostrophic potential

vorticity ('pseudo-potential vorticity') equation, and inferred the existence and spectral form of an inertial subrange in quasigeostrophic motion from the results of Kraichnan (1967) on two dimensional Navier-Stokes turbulence. In this subrange, enstrophy (half-squared vorticity) is cascaded to small scales, rather than energy as in three-dimensional turbulence. Charney (1971) introduced the phrase 'geostrophic turbulence' to describe the energetic, low frequency, high wavenumber, three-dimensional, near-geostrophic motions to which this theory applies. The phrase is now also used more generally to describe the 'chaotic, nonlinear motion of fluids that are near to a state of geostrophic and hydrostatic balance' (Rhines, 1979) but in which anisotropic waves (e.g., Rossby waves) may also propagate.

In the predicted inertial subrange, the energy spectrum E(k) has the form

$$E(k) = C\,\eta^{2/3}\,k^{-3},$$

where C is a universal constant, η is the enstrophy cascade rate, and k is an isotropic wavenumber. Total energy is equally distributed between the potential energy and each of the two components of kinetic energy. For a spatially oriented wavenumber (e.g., wavenumber along a tow track), the power law dependence is unchanged, but the transverse velocity kinetic energy component contains three times the

energy of each of the longitudinal component and the potential energy component, so the total energy is five times the potential energy (Charney, 1971).

The potential energy may be expressed in terms of the density, using the hydrostatic balance and a local value of the buoyancy frequency N:

$$\text{(Potential energy)} = (g/N)^2((\rho - \rho_0)/\rho_0)^2,$$

where g is gravitational acceleration, ρ is density, and ρ_0 is a constant reference density. Temperature and salinity data (Figure II.2) indicate that relative temperature tends to determine relative density, at least on the 10-15 km scales of the salinity data. We have used linear regression T-S relations from these data to convert 15 m temperature to density. For Tow 1, a single linear T-S relation was used, for Tow 2, three relations, for Tow 3, a single relation, and for Tow 4, three relations. The change in spectral shape from this conversion was minimal. The spectral levels were altered, with Tows 2 and 3 nearly equal and Tow 1 roughly half, Tow 4 roughly three times as large as Tows 2 and 3. (The large front near 26^o N is intensified by the conversion to density and was excluded from the density spectra, as it imparts a strong k^{-2} signal to the spectrum and appears to belong to a dynamical regime different from that of the remainder of the observations.)

A relatively large uncertainty is associated with the choice of a value of N for the conversion from density to potential energy. The Charney theory requires use of the local N, which is assumed to be slowly varying. In the mixed layer, N may be arbitrarily small, and at the mixed layer base, N is not slowly varying. We use a moderate value of 2 cph. Within the 95% confidence intervals, the resulting ensemble averaged potential energy spectrum may be obtained directly by multiplying the 15 m temperature spectrum in Figure II.10 by 10^3 cm s^{-2} $^oC^{-2}$. The variance in the 0.1-1 cpkm band is roughly 3 cm^2 s^{-2}, the corresponding predicted kinetic energy 12 cm^2 s^{-2}. A velocity scale U formed from the square root of twice the kinetic energy is 5 cm s^{-1}, which yields a Rossby number ($Uk/f = 0.05$ at $k = 0.1$ cpkm) that is appropriate for quasigeostrophic theory. Assuming the universal constant C is equal to one, we estimate the potential enstrophy transfer (dissipation) rate η as 2×10^{-16} s^{-3}. This lies between atmospheric estimates of 10^{-15} s^{-3} (Charney, 1971; Leith, 1971) and numerical ocean model values of 5×10^{-19} s^{-3} (McWilliams and Chow, 1981).

The interpretation of the 0.1-1 cpkm band as a geostrophically turbulent inertial subrange appears to be consistent with the theory. There is considerable uncertainty in the conversion of temperature to density and potential energy. The predictive theory requires a slowly

varying N and a flow isolated from boundary effects; these conditions may not apply here, but it is not evident that they are essential to the dynamics. The rms temperature amplitude (square root of the variance) in the band is roughly 0.05 ^{o}C. This is 50 times the thermistor noise level, but it is a small physical signal that could be created by relative meridional displacements of five to ten kilometers in the mean field. Some possible alternative mechanisms are:

(1) Internal waves. At 15 m depth, horizontal displacements by high frequency internal waves should be small. Lagrangian motion due to near-inertial waves and wind-driven surface currents, which will depend strongly on the horizontal structure of the velocity fields, is not well understood and may contribute to the observed variance.

(2) Variations in air-sea fluxes and entrainment. At horizontal scales below 10 km, variations in air-sea fluxes should not be sufficient to create 0.05 ^{o}C features in a mixed layer of 75-125 m depth. (This would require a differential heat flux of 200 W m^{-2} over a day.) Note that variations in mixed layer depth may produce temperature variations in response to even a spatially constant heat flux. Variations in entrainment, such as those observed by Large et al. (1986), similarly may produce mixed layer

temperature variations, but again presumably mostly on scales larger than 10 km.

Over 900-km space and two-week time scales and despite variable atmospheric conditions, the spectral shapes were roughly constant. This suggests that processes that contribute substantially to the variance must be statistically homogeneous over these scales. Near-inertial currents, which respond strongly to storms, would appear not to meet this criterion.

Finally, we note that the -3 power law temperature spectrum differs from that predicted for a passively advected scalar in a turbulent flow. In that case the scalar spectrum, not the gradient spectrum, is inversely proportional to wavenumber (Batchelor, 1959).

II.6 Summary

The thermistor tows yield a detailed two-dimensional description of surface layer temperature along 1400 km of tow tracks in the Eastern North Pacific Subtropical Frontal Zone during January 1980. In brief, we find:

(1) The dominant features have wavelengths of 10-100 km, amplitudes of 0.2 to 1.0 ^{o}C, and no preferred orientation with respect to the mean meridional gradient (Figure II.4). These features, which could be created from the climatological mean sea surface temperature field by

adiabatic meridional displacements of roughly 100 km, likely arise from baroclinic instability of the geostrophic upper ocean flow. They form a plateau in the temperature gradient spectrum at wavelengths above 10 km (Figure II.8).

(2) Strong temperature fronts are observed near 33° N, 31° N and 27° N, with density compensation by salinity increasing northward (Figures II.3,4). Maximum horizontal near-surface gradients exceed 0.25 °C/100 m (Figure II.7). There is evidence of vertically differential horizontal advection in the surface layer by light winds (Figure II.5b), enhanced vertical mixing during periods of strong winds, and shallow (100-200 m depth) convection caused by wind-driven advection of a dense layer over a deep less-dense layer.

(3) Temperature is roughly normally distributed around the climatological mean (Figure II.6). The near-surface horizontal temperature gradient has high kurtosis (Figure II.7).

(4) The high horizontal wavenumber (0.1-1 cpkm) tail of the near-surface temperature spectrum has the -3 power law form (Figures II.8,10) predicted by Charney (1971) for energetic high wavenumber near-geostrophic motion above a baroclinic production range. Horizontal temperature gradients have significant vertical coherence over the upper 50 m at all wavelengths and over the upper 70 m at wavelengths greater than 5 km (Figure II.12).

(5) The departure at 70 m depth of the temperature spectrum from the -3 power law can be ascribed to internal wave vertical displacements that are consistent with the Garrett-Munk model of the internal wave spectrum (Figure II.11).

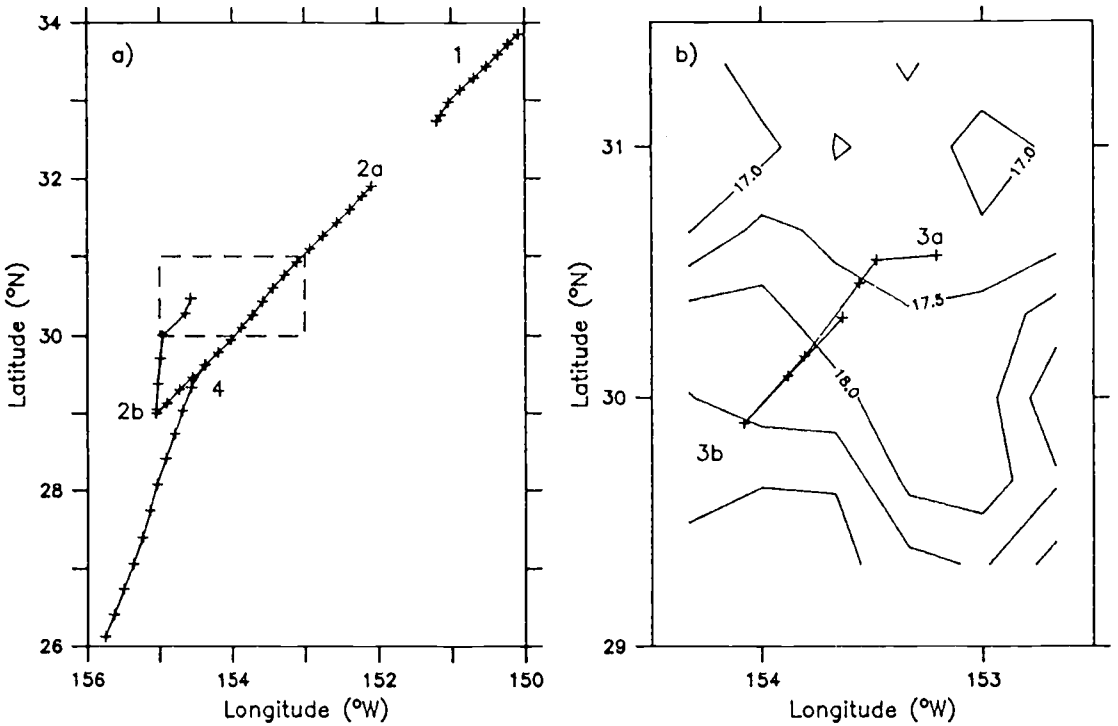

Figure II.1 Tow tracks. + -- two-hourly positions. (Table 1 lists start and finish positions and times.)
a) Tows 1, 2a, 2b, and 4. Ship remained within dashed rectangle during 19-26 Jan.
b) Tows 3a and 3b. Isotherms at 20 m from CTD survey (Roden, 1981).

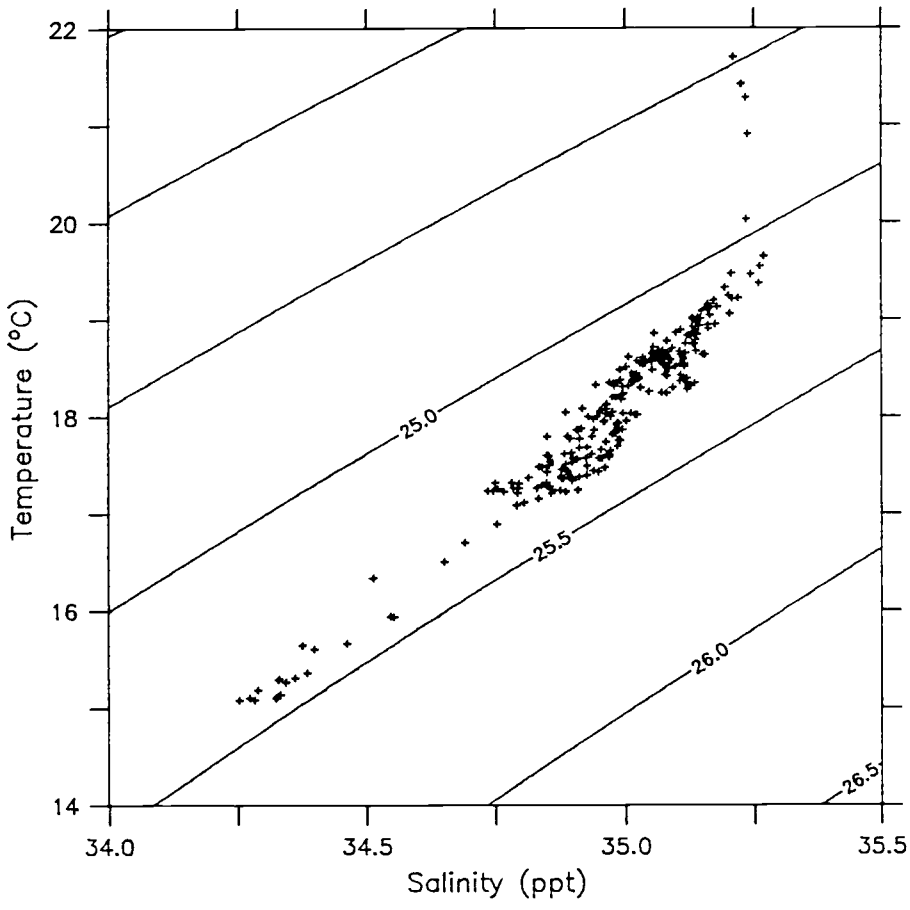

Figure II.2 Hourly sea surface temperature vs. salinity from on-board CTD during 16-28 Jan., with contours of σ_t.

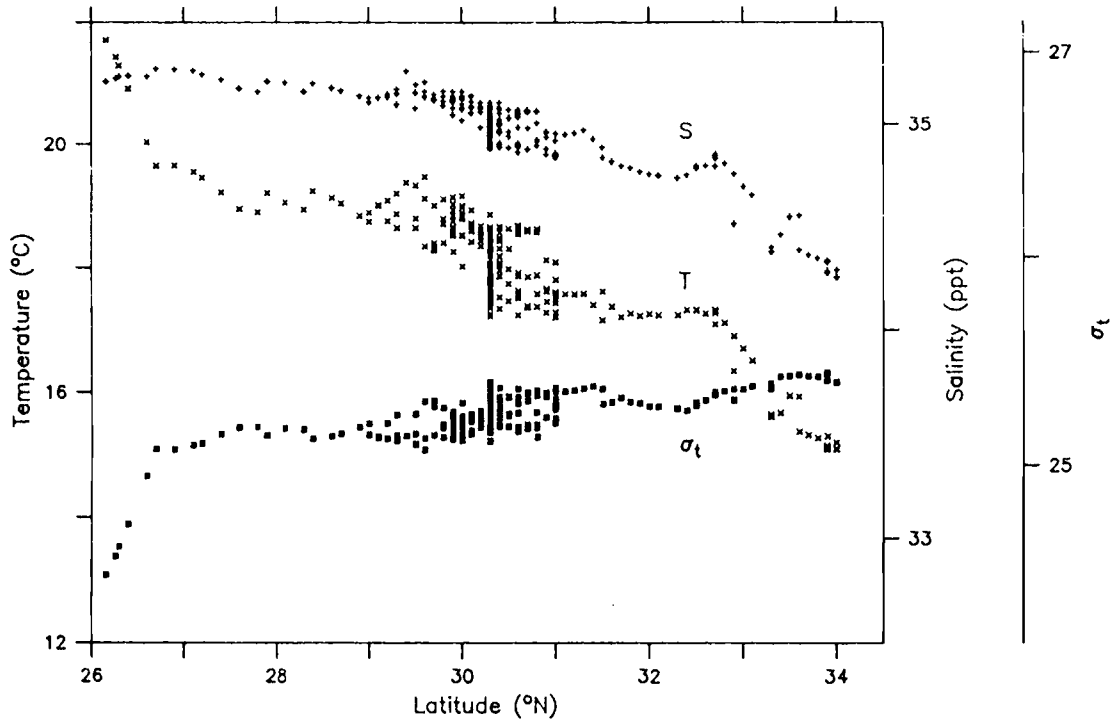

Figure II.3 Hourly sea surface temperature, salinity and σ_t from on-board CTD vs. latitude.

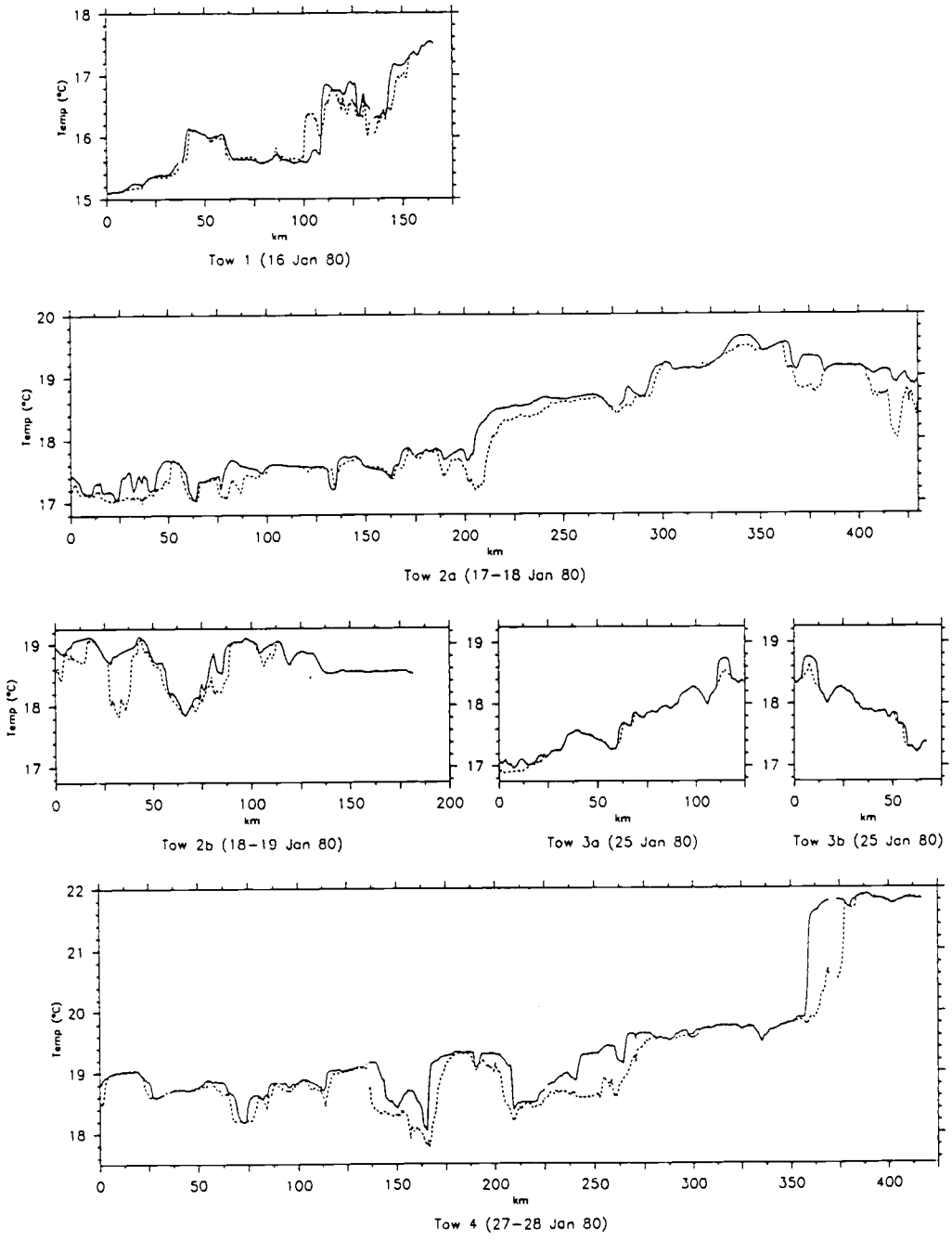

Figure II.4 Nominal 15 m (solid) and 70 m (dashed) thermistor temperature (horizontal 500 m means) vs. distance along tow tracks. The large fronts in Tow 1 near 125 km, Tow 2a near 200 km, and Tow 4 near 350 km are visible in Figure 3 near 33° N, 31° N, and 27° N, respectively.

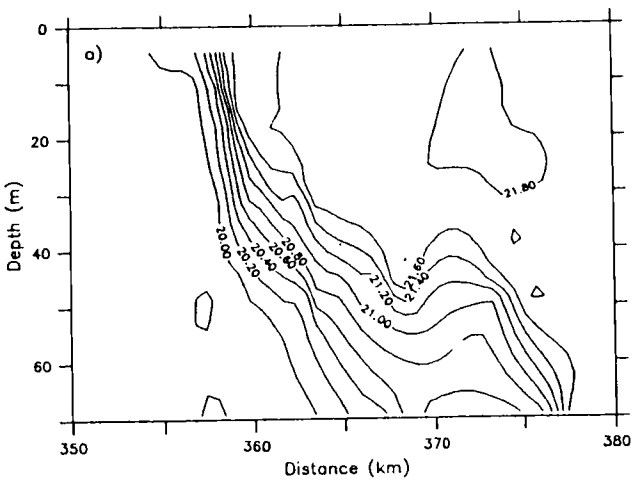

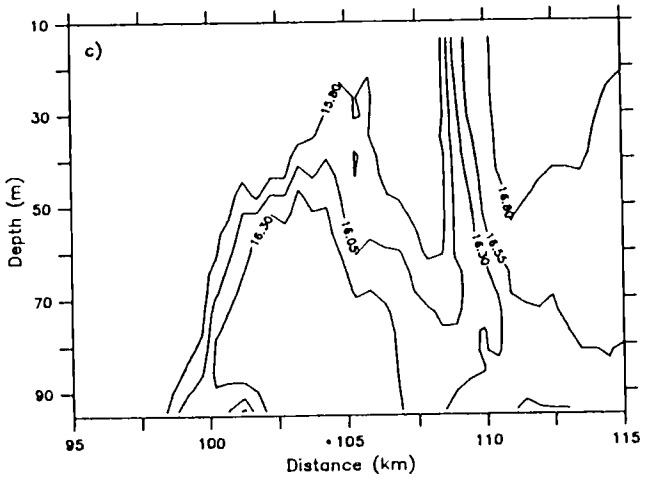

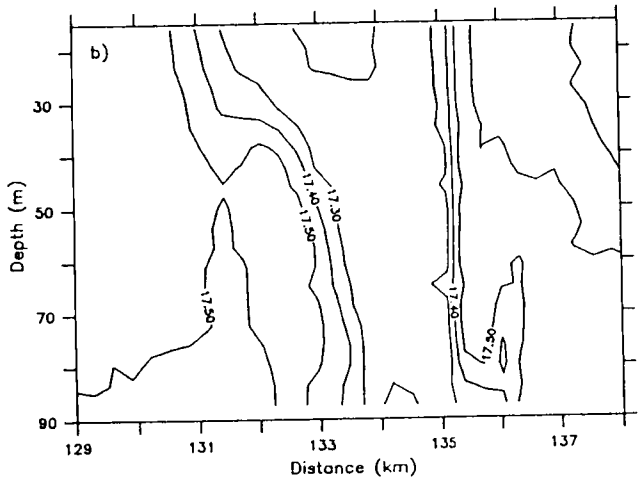

Figure II.5

Examples of fronts shown by isotherm cross-sections (interpolated from horizontal 100 m mean thermistor temperatures) vs. depth and distance along tow tracks. a) Tow 4. This front is visible in Figure 3 near 27° N. b) Tow 2a. c) Tow 1.

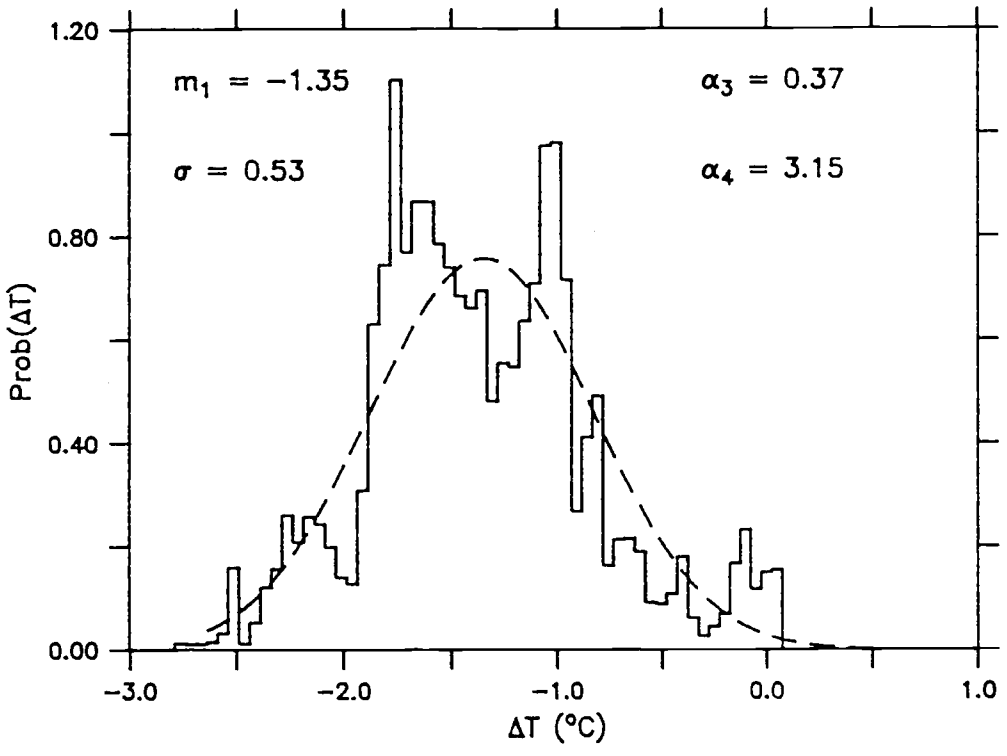

Figure II.6 Probability density of difference of 15 m temperature from climatological surface temperature. Area under curve is fraction of occurrence. Dashed line: Gaussian distribution with same mean and standard deviation.

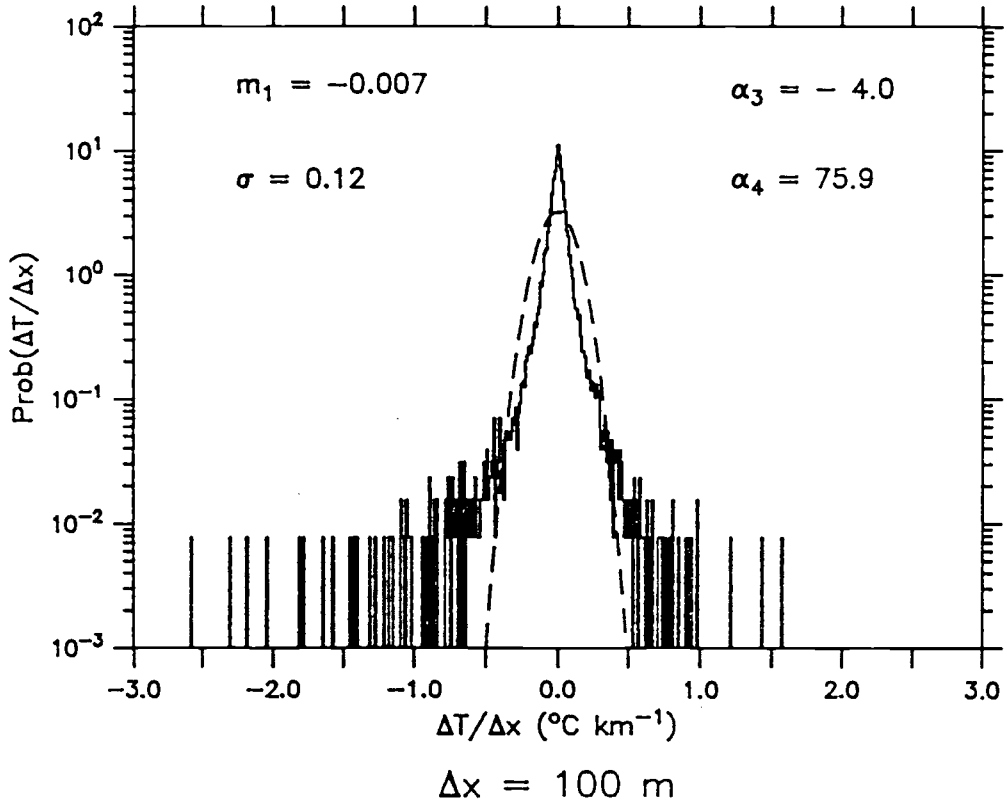

Figure II.7 Probability density of 15 m horizontal temperature gradient. Area under curve is fraction of occurrence. Dashed line: Gaussian distribution with same mean and standard deviation.

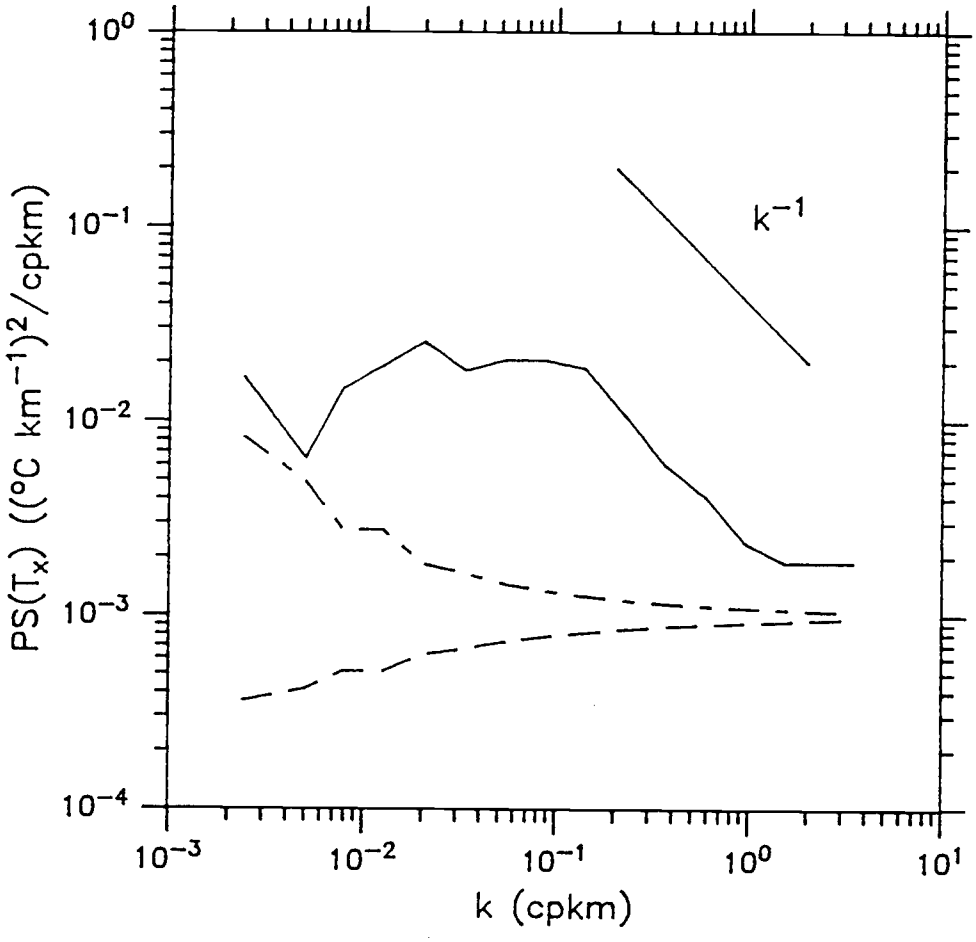

Figure II.8 Horizontal wavenumber spectrum of horizontal temperature gradient from Tows 1, 2a, 2b, 3a, and 4, ensemble averaged and band averaged to 5 bands per decade. Slope of -1 power law indicated. Dashed lines: 95% confidence intervals.

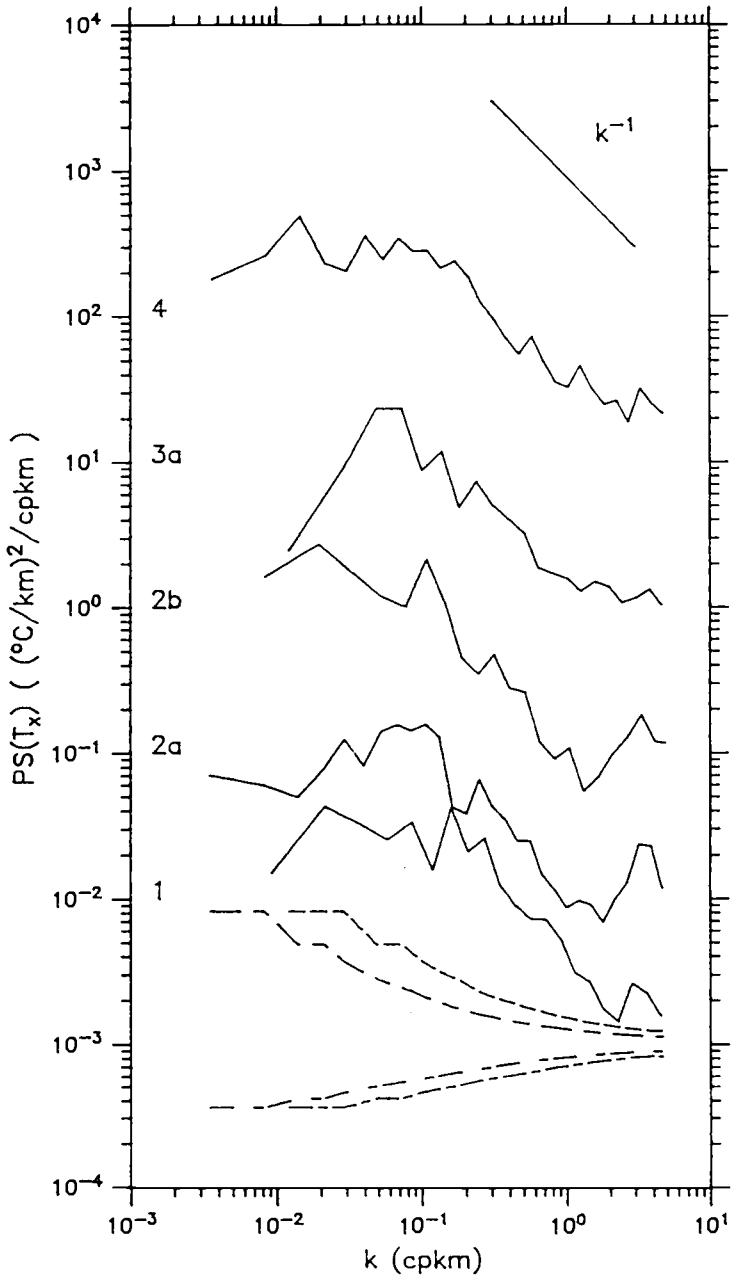

Figure II.9 Horizontal wavenumber spectra of horizontal temperature gradient from Tows 1, 2a, 2b, 3a, and 4, band averaged to 10 bands per decade. Successive spectra are offset by one decade. Slope of -1 power law indicated. Dashed lines: 95% confidence intervals for shortest (Tow 3a) and longest (Tow 2a) records.

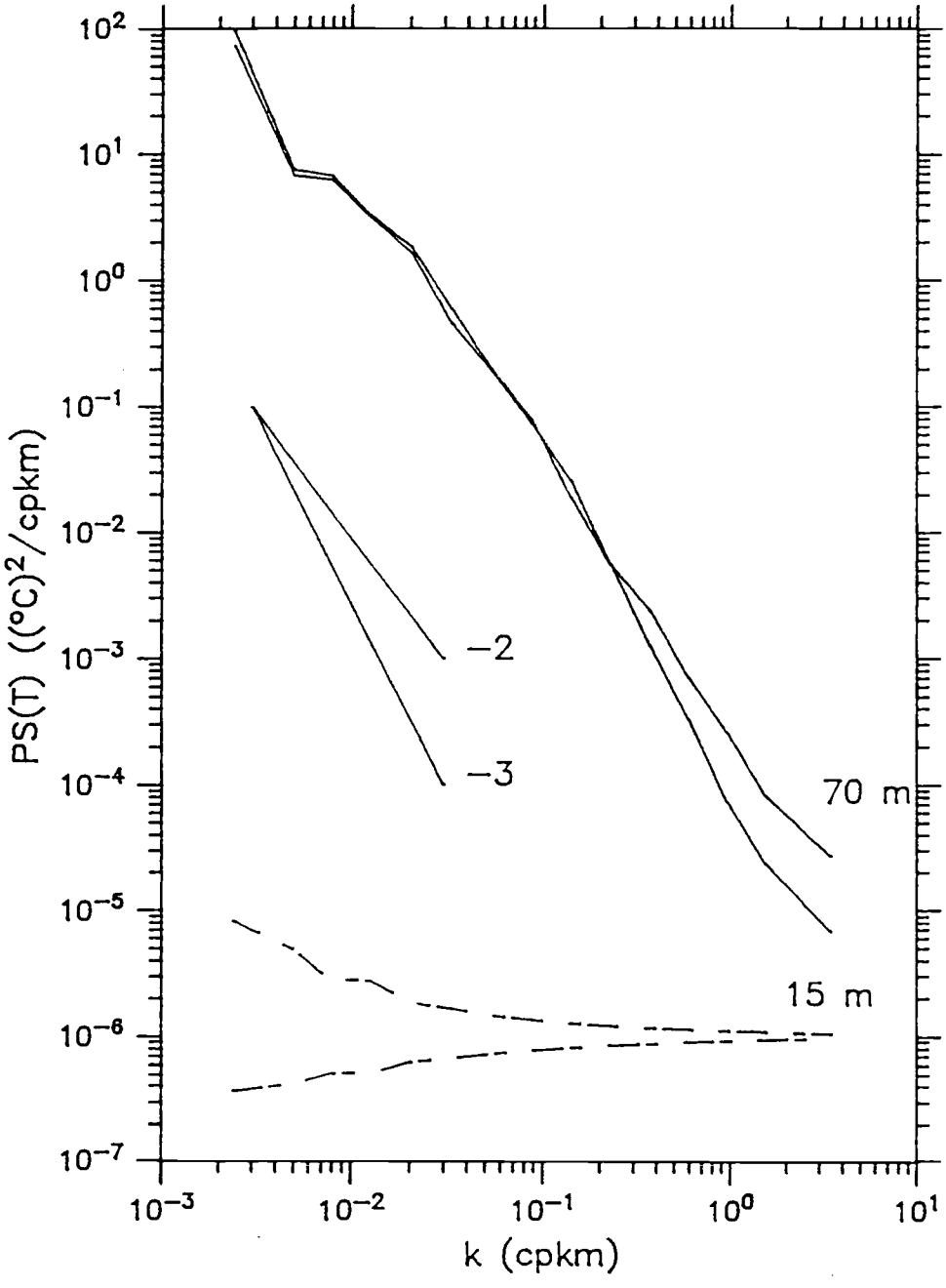

Figure II.10 Horizontal wavenumber spectra of 15 m and 70 m temperature for Tows 1, 2a, 2b, 3a, and 4, ensemble averaged and band averaged to 5 bands per decade. Slope of -2 and -3 power laws are indicated. Dashed lines: 95% confidence intervals.

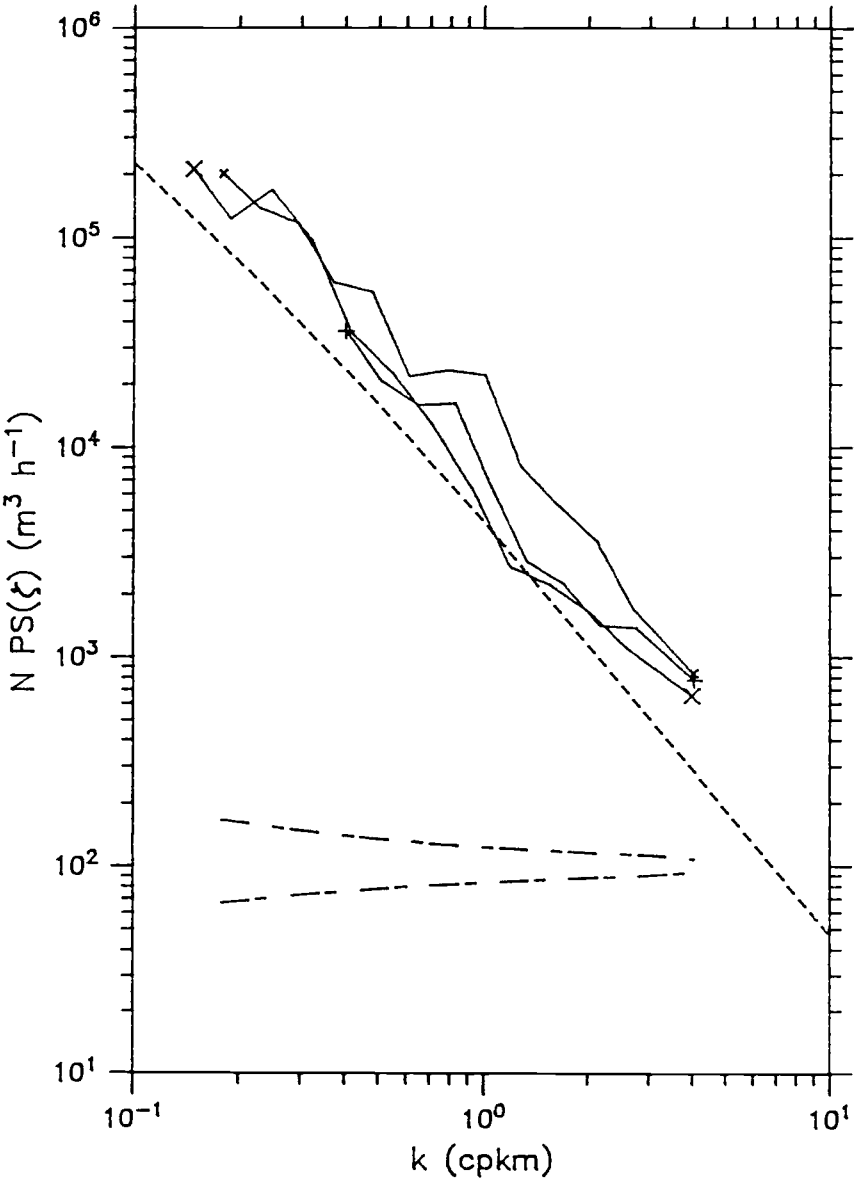

Figure II.11 Estimated 70 m internal wave vertical displacement spectra from difference of 70 m and 15 m power spectra, band averaged to 10 bands per decade (solid lines: x -- Tow 2a, + -- Tow 2b, X -- Tow 4). 95% confidence intervals (long dashes); Garrett-Munk canonical internal wave spectrum with r = 320 m^2 h^{-1}, t = 4 x 10^{-4} cph cpm^{-1} (short dashes).

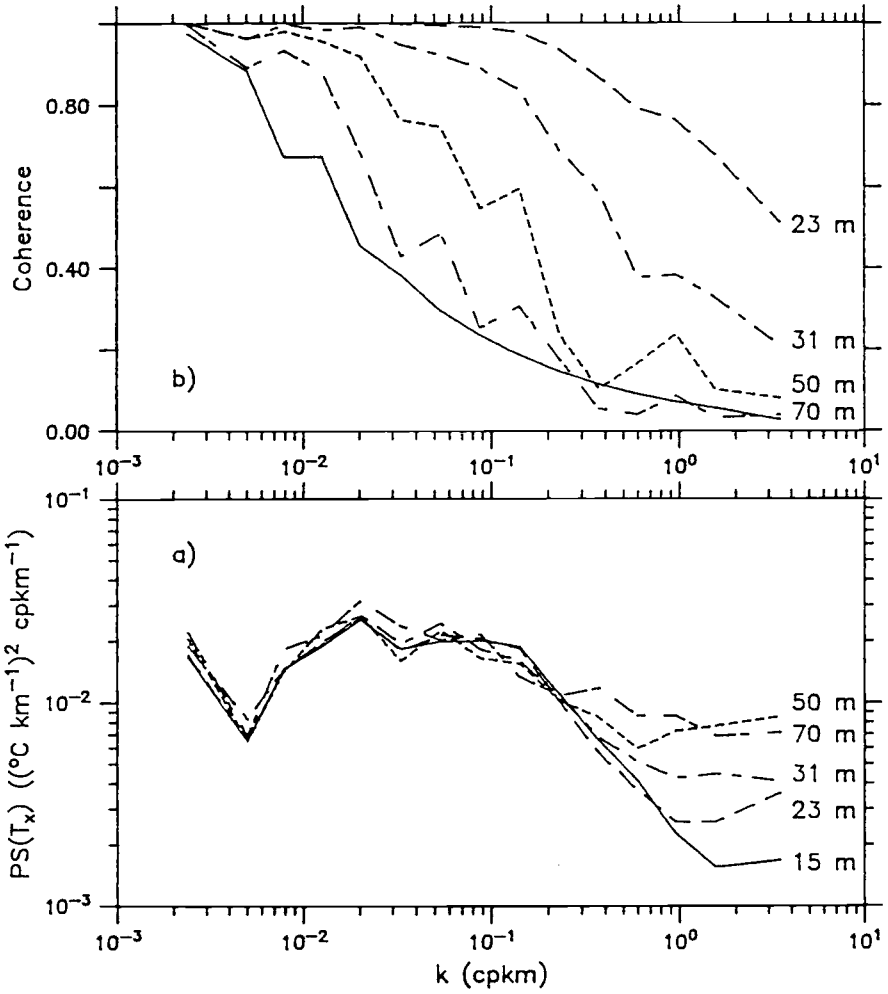

Figure II.12 Horizontal wavenumber spectra and coherence, ensemble averaged and band averaged to 5 bands per decade. a) Spectra of horizontal temperature gradient at 15, 23, 31, 50, and 70 m. (95% confidence intervals as in Figure 8) b) Dashed lines: Coherence from cross-spectra between 15 m and 23, 31, 50, and 70 m horizontal temperature gradients. Solid line: 95% significance level for non-zero coherence.

Table II.1 Tow start and finish positions and times.

Tow	Time (GMT)	N. Latitude	W. Longitude
1	0040 16 Jan	33° 51′	150° 05′
	1600 16 Jan	32° 44′	151° 12′
2a	0520 17 Jan	31° 54′	152° 05′
b	1655 18 Jan	29° 00′	155° 03′
	0245 19 Jan	30° 28′	154° 38′
3a	0700 25 Jan	30° 34′	153° 12′
b	1312 25 Jan	29° 53′	154° 05′
	1700 25 Jan	30° 19′	153° 38′
4	1900 27 Jan	29° 38′	154° 24′
	1650 28 Jan	26° 07′	155° 45′

Table II.2 Winds and surface fluxes. Winds are daily vector averages of hourly observations. Fluxes are positive downward.

Day	Wind		Heat	Buoyancy	Monin-Obukhov
	Spd.	Dir.	Flux	Flux	Depth
(Jan 1980)	($m\ s^{-1}$, ^{o})		($W\ m^{-2}$)	($10^{-8}\ m^2\ s^{-3}$)	(m)
16	9	250	95	5.2	69
17	10	200	82	4.7	62
18	9	260	-25	-2.6	
19	13	310	-69	-6.2	
20	8	230	-19	-1.9	(rain, half day)
21	7	260	92	4.8	54
22	11	340	(no radiation measurement)		
23	10	340	-27	-3.2	
24	6	000	6	-0.9	
25	6	020	43	1.5	77
26	4	240	-14	-1.6	(rain, half day)
27	5	330	75	3.5	24
28*	8	120	70	3.1	77

*Last observation at 1700 28 January.

Table II.3 Climatological sea surface temperature (°C), averaged over 150-155° W.

Month	N. Latitude		
	25°	30°	35°
January	22.6	19.8	16.0
February	22.3	19.3	15.4

II.7 References

Batchelor, G. K., 1959. Small-scale variation of convected quantities like temperature in a turbulent fluid, part 1. J. Fluid Mechanics, 5:113-139

Charney, J. G., 1971. Geostrophic Turbulence, J. Atmos. Sci., 28:1087-1095

Desaubies, Y. J. F., 1976. Analytical Representation of Internal Wave Spectra, J. Phys. Oceanogr., 6:976-981

Garrett, C. and W. Munk, 1972. Space-Time Scales of Internal Waves, Geophys. Fluid Dyn., 2:225-264

Katz, E. J. and M. G. Briscoe, 1979. Vertical Coherence of the Internal Wave Field from Towed Sensors, J. Phys. Oceanogr., 9:518-530

Kraichnan, R. H., 1967. Inertial Ranges in Two-Dimensional Turbulence, Phys. Fluids, 10:1417-1423

Kunze, E. and T. B. Sanford, 1984. Observations of Near-Inertial Waves in a Front, J. Phys. Oceanogr., 14:566-581

Large, W. G., J. C. McWilliams, and P. P. Niiler, 1986. Upper Ocean Thermal Response to Strong Autumnal Forcing of the Northeast Pacific, J. Phys. Oceanogr., 16:1524-1550

Lativ, M., 1987. Tropical Ocean Circulation Experiments, J. Phys. Oceanogr., 17:246-263

Leith, C. E., 1971. Atmospheric Predictability and Two-Dimensional Turbulence, J. Atmos. Sci., 28:145-161

McWilliams, J. C. and J. H. S. Chow, 1981. Equilibrium Geostrophic Turbulence I: A Reference Solution in a Beta-Plane Channel, J. Phys. Oceanogr., 11:921-949

Monin, A. S. and A. M. Yaglom, 1975. Statistical Fluid Mechanics, Vol. 2, MIT Press, Cambridge

Niiler, P. P., and R. W. Reynolds, 1984. The Three-Dimensional Circulation near the Eastern North Pacific Subtropical Front, J. Phys. Oceanogr., 14:217-230

Paulson, C. A., R. J. Baumann, L. M. deWitt, T. J. Spoering, and J. D. Wagner, 1980: Towed Thermistor Chain Observations in FRONTS 80, Oregon State University School of Oceanography Data Report 85, Reference 80-18.

Rhines, P. B., 1979: Geostrophic Turbulence, Ann. Rev. Fluid. Mech., 11:401-441

Robinson, M. K., 1976: Atlas of North Pacific Ocean Monthly Mean Temperatures and Mean Salinities of the Surface Layer, Naval Oceanographic Office Reference Publication 2.

Roden, G. I., 1973: Thermohaline Structure, Fronts, and Sea-Air Exchange of the Trade Wind Region east of Hawaii, J. Phys. Oceanogr., 4:168-182

Roden, G. I., 1975: On North Pacific Temperature, Salinity, Sound Velocity and Density Fronts and their Relation to the Wind and Energy Flux Fields, J. Phys. Oceanogr., 5:557-571

Roden, G. I., 1981: Mesoscale Thermohaline, Sound Velocity and Baroclinic Flow Structure of the Pacific Subtropical Front During the Winter of 1980, J. Phys. Oceanogr., 11:658-675

Van Woert, M., 1981: Satellite Observations in FRONTS 80, SIO Reference No. 81-38.

Van Woert, M., 1982: The Subtropical Front: Satellite Observations During FRONTS 80, J. Geophys. Res., 87C:9523-9536

III. SEMIGEOSTROPHIC WIND-DRIVEN THERMOCLINE UPWELLING AT A COASTAL BOUNDARY

Abstract

We formulate analytically and solve numerically a semigeostrophic model for wind-driven thermocline upwelling. The model has a variable-density entraining mixed layer and two homogeneous interior layers. All variables are uniform alongshore. The wind stress and surface heating are constant. The system is started from rest, with constant layer depths and density differences. A modified Ekman balance is prescribed far offshore, and the normal-to-shore velocity field responds on the scales of the effective local internal deformation radii, which themselves adust in response to changes in layer depths, interior geostrophic vorticity, and mixed layer density. Sustained upwelling results in a step-like horizontal profile of mixed layer density, as the layer interfaces "surface" and are advected offshore. The upwelled horizontal profile of mixed layer density scales with the initial internal deformation radii. Around the fronts, surface layer divergence occurs that is equal in magnitude to the divergence in the upwelling zone adjacent to the coast, but its depth penetration is inhibited by the stratification.

III.1 Introduction

In this chapter we combine a simple representation of a stratified interior with a previously-developed theory for strong horizontal gradients in a surface mixed layer (de Szoeke and Richman, 1984) to develop a model for the wind-driven upwelling of a stratified fluid. We apply the model to the case of coastal upwelling. The interior consists of two homogeneous layers of differing density. The mixed layer resolves the fronts that form as layer interfaces "surface" at the coast and are advected offshore. Combining these elements allows the modelling of the upwelling and entrainment into the surface layer of deep, dense interior fluid that is initially separated from the surface layer by an intermediate layer of less-dense fluid.

We employ two principal analytical simplifications: we specify that all flow variables be uniform in the alongshore direction, and that semigeostrophic dynamics apply. These semigeostrophic equations are similar to those developed by Hoskins and Bretherton (1972) for the study of atmospheric frontogenesis (subsequently generalized to three dimensions by Hoskins (1975)). They were used by Pedlosky (1978) in an adiabatic model of the onset of upwelling driven by a mass sink at the coast and an alongshore pressure gradient.

The present model includes an entraining, diabatic surface mixed layer with variable density. The flow is driven by an alongshore wind stress and surface heating. A modified Ekman balance forces surface layer fluid offshore and interior fluid onshore, causing a surface divergence and upwelling of isopycnals near the coastal boundary. The horizontal scale of this divergence is allowed to adjust dynamically by careful consideration of the normal-to-shore momentum balance. The model is inviscid (except for the viscosity implicit in the vertical mixing in the surface layer).

We solve the reduced equations numerically. Initially, the layer depths and surface layer density are constant, and the horizontal scale of the surface divergence is determined by a single internal deformation radius. After the mixed layer base "surfaces" near the coast and the upwelled front propagates offshore, there are two zones of surface layer transport divergence. One of these is associated with the coastal boundary, the other with the upwelled front.

The surface divergence has comparable magnitude in these two zones. At the front, the divergence is associated only with deformations of the mixed layer base, and does not penetrate beyond the uppermost interior layer. At the boundary, the divergence is associated with upwelling of both

interior layers, on the horizontal scale of the local internal deformation radius.

The uppermost interior layer eventually becomes entrained completely into the surface layer in the upwelling region, leaving only two layers there. We derive matching conditions to join the two-layer region with the three-layer region. Sustained upwelling results in a step-like horizontal profile of surface layer density, as the interior layer interface "surfaces" and is advected offshore as a front in the surface layer. The upwelled horizontal density profile scales with an internal deformation radius calculated from the initial fields.

III.2 Model formulation

III.2.a Equations

Figure III.1 displays the model geometry. We use a right-handed Cartesian coordinate system with origin at the surface on the coastal boundary, x alongshore, y positive offshore, and z vertical. We specify that all flow variables be uniform in the alongshore direction and take the flow to be governed by the semigeostrophic equations (e.g., Pedlosky, 1979, Sec. 8.4): the geostrophic balance holds normal to shore, while the alongshore acceleration is retained at lowest order. The main effect of imposing semigeostrophy is

to remove the inertio-gravity waves. The momentum and continuity equations are, in the surface mixed layer (layer 1),

$$u_{1t} + v_1 u_{1y} - fv_1 = \tau_z/\rho_0 = (\tau^x - \tau_e)/\rho_0 h_1, \tag{1a}$$

$$fu_1 = - \langle p_{1y} \rangle/\rho_0, \tag{1b}$$

$$p_{1z} = - g\rho_1(y,t), \tag{1c}$$

$$v_{1y} + w_{1z} = 0, \tag{1d}$$

and in the interior layers (layers 2 and 3),

$$u_{it} + v_i u_{iy} - fv_i = 0, \tag{2a}$$

$$fu_i = - p_{iy}/\rho_0, \tag{2b}$$

$$p_{iz} = - g\rho_i. \tag{2c}$$

$$v_{iy} + w_{iz} = 0, \qquad i=2,3. \tag{2d}$$

Here (u_i,v_i,w_i) are the (x,y,z) components of velocity and ρ_i is density in layer i, i = 1,2,3, p is pressure, h_1 is the depth of the mixed layer, ρ_0 is a constant reference density, f is the Coriolis parameter, and g is the acceleration of gravity. Subscripts x, y, and z denote partial differentiation. The upper layer density ρ_1 is allowed to vary with y and t, while the interior layer densities are constant. The angle brackets around the upper layer pressure gradient denotes a vertical average through the mixed layer. This allows the neglect of the vertical shear that is associated with horizontal density gradients through the thermal wind relation. (This procedure can be justified as in de Szoeke and Richman (1984) by an expansion in orthogonal

polynomials in z.) The vertical momentum balance is hydrostatic. The alongshore geostrophic velocity in the mixed layer is accelerated inertially and by the wind stress τ^x and decelerated by the entrainment stress τ_e. A small layer immediately below the mixed layer, in which fluid being entrained from the interior is accelerated and through which the stress falls smoothly to zero, has been neglected (see Niiler, 1975). The interior geostrophic velocities are accelerated inertially.

The variable upper layer density satisfies the thermodynamic equation,

$$\rho_{1t} + v_1\rho_{1y} = [-\alpha Q/c + (\rho_I - \rho_1)w_e]/h_1 \qquad (3)$$

where Q is net heating, c is specific heat, and α is thermal expansibility. The subscript I indicates an interior layer variable that is evaluated immediately below the base of the mixed layer. (Under certain conditions layer 3 may come in contact with the mixed layer, so that ρ_I will not always be ρ_2.) The effect of salinity on density could easily be included also, but we neglect it for simplicity.

The entrainment velocity w_e is obtained by the energy argument of Kraus and Turner (1967). This balances the energy input from the wind, minus the potential energy removed by surface heating, with the potential energy created by entrainment of dense interior fluid into the mixed layer:

$$m_0\rho_0 u_*^3 - (1/2)gh_1\alpha Q/c = (1/2)w_e g(\rho_I - \rho_1)h_1. \qquad (4)$$

The energy input from wind stirring is taken as proportional to the cube of the friction velocity u_*, with m_0 an empirical proportionality constant of order one. For simplicity, we neglect shear-driven deepening. Negative entrainment velocities and detrainment are not allowed, so the expression for w_e is,

$$w_e = \max \{ \ (2m_0\rho_0 u_*^3 - gh_1\alpha Q/c)[g(\rho_I - \rho_1)h_1]^{-1}, \ 0 \}. \quad (5)$$

Since water being entrained into the mixed layer from the interior must be accelerated to the velocity of the mixed layer, an entrainment stress τ_e arises. This stress is the flux of momentum deficit into the mixed layer,

$$\tau_e = \rho_0(u_1 - u_I)w_e. \quad (6)$$

In keeping with the assumption that geostrophic velocities are large relative to ageostrophic velocities, the ageostrophic momentum deficit flux is neglected.

The small horizontal scales to be considered (see Section III.2c) justify the rigid lid approximation, so the layer depths satisfy,

$$h_1 + h_2 + h_3 = H, \quad (7)$$

where H is the constant total fluid depth.

Integration of the continuity equations (1d) and (2d), with the requirements that normal velocity be continuous at layer interfaces and vertical velocity vanish at the top and bottom boundaries, yields prognostic equations for the layer depths,

$$h_{1t} + (h_1 v_1)_y = w_e, \tag{8a}$$

$$h_{2t} + (h_2 v_2)_y = - w_e, \tag{8b}$$

$$h_{3t} + (h_3 v_3)_y = 0. \tag{8c}$$

If layer 2 vanishes in a region, so that layer 3 comes in contact with the mixed layer, the entrainment velocity must be subtracted from the layer 3 depth evolution equation. In this case the layer depth evolution equations are,

$$h_{1t} + (h_1 v_1)_y = w_e, \tag{9a}$$

$$h_{3t} + (h_3 v_3)_y = - w_e. \tag{9b}$$

Note that the base of the mixed layer is not a material surface; fluid may pass (upward) through it. De Szoeke (1981) gives a careful discussion of the form of these equations. Addition of (8a-c) and integration from the coastal boundary, where normal velocities must vanish, yields the condition of no net offshore mass flux,

$$h_1 v_1 + h_2 v_2 + h_3 v_3 = 0. \tag{10}$$

This holds as well if h_2 is equal to zero.

When layer 3 is isolated from the mixed layer, potential vorticity in layer 3 is conserved following the motion, that is,

$$P_{3t} + v_3 P_{3y} = 0, \tag{11a}$$

where

$$P_3 = (f - u_{3y})/h_3 \tag{11b}$$

is the potential vorticity in layer 3. This may be verified by direct differentiation and the use of (2a) and (8c). It

follows from (2a) and (8b) that the potential vorticity in layer 2,

$$P_2 = (f - u_{2y})/h_2, \tag{12a}$$

obeys the equation,

$$P_{2t} + v_2 P_{2y} = w_e P_2/h_2. \tag{12b}$$

Similarly, when layer 3 is in contact with the mixed layer, so that (9b) holds instead of (8c), P_3 obeys,

$$P_{3t} + v_3 P_{3y} = w_e P_3/h_3, \tag{13}$$

instead of (11a).

Vertical integration of the hydrostatic equations yields, in the three-layer domain,

$$p_1 = p_0(y,t) - gz\rho_1(y,t), \tag{14a}$$

$$p_2 = p_0(y,t) - g[\rho_2 - \rho_1(y,t)]h_1(y,t) - g\rho_2 z, \tag{14b}$$

$$p_3 = p_0(y,t) - g[\rho_3 - \rho_1(y,t)]h_1(y,t) - g(\rho_3 - \rho_2)h_2(y,t) - g\rho_3 z, \tag{14c}$$

where $p_0(y,t)$ is surface pressure. In the two-layer domain, (14c) holds with $h_2 = 0$, and (14b) is neglected. Inserting (14) into the geostrophic relations (1a) and (2a) yields the thermal wind relations,

$$\rho_0 f(u_1 - u_2) = - g[(\rho_2 - \rho_1)h_{1y} + (1/2)h_1(\rho_2 - \rho_1)_y], \tag{15a}$$

$$\rho_0 f(u_2 - u_3) = - g(\rho_3 - \rho_2)(h_1 + h_2)_y = g(\rho_3 - \rho_2)h_{3y}, \tag{15b}$$

or, in the two-layer domain,

$$\rho_0 f(u_1 - u_3) = - g[(\rho_3 - \rho_1)h_{1y} + (1/2)h_1(\rho_3 - \rho_1)_y]. \tag{15c}$$

Equations (1a) and (2a) are dynamic equations for the geostrophic momentum in each layer. Equation (3) is a thermodynamic equation for the mixed layer density. Equations (8) or (9) are kinematic equations for the layer depths. These evolution equations all depend on the ageostrophic velocities v_i. However, there is no evolution equation for the v_i, since their time derivatives have been eliminated by the semigeostrophic approximation. Since the geostrophic shear (15) depends only on the layer depths and densities, the rate of change of the geostrophic shear may be calculated in two different ways: either directly, from the momentum equations (1a) and (2a), or indirectly, from the kinematic and thermodynamic equations (3) and (8) or (9) for the layer depths and mixed layer density. This calculation yields consistency relations that the ageostrophic velocities v_i must satisfy at each time in lieu of the missing evolution equations. These relations take the form of differential equations in y. In the three-layer domain, taking a time derivative of (15a,b) and substituting (1a), (2a), (3), (6), and (8) yields,

$$g(\rho_0 f)^{-1}[(\rho_2 - \rho_1)h_1{}^2 v_{1y}]_y - h_1(f - u_{2y})(v_1 - v_2)$$
$$= \tau^x/\rho_0 + g(2\rho_0 f)^{-1}\{h_1[\alpha Q/c + (\rho_2 - \rho_1)w_e]\}_y, \quad (16a)$$

$$g(\rho_0 f)^{-1}(\rho_3 - \rho_2)(h_3 v_3)_{yy}$$
$$+ (f - u_{2y})v_2 - (f - u_{3y})v_3 = 0. \quad (16b)$$

In the two-layer region, the single resulting equation is,

$$g(\rho_0 f)^{-1}[(\rho_3 - \rho_1)h_1^2 v_{1y}]_y - h_1(f - u_{3y})(v_1 - v_3)$$
$$= \tau^x/\rho_0 + (2\rho_0 f)^{-1}\{h_1[\alpha Q/c + (\rho_3 - \rho_1)w_e]\}_y. \qquad (16c)$$

These equations are supplemented by the boundary conditions

$$v_1 = v_2 = v_3 = 0, \quad y = 0, \qquad (17a)$$

$$v_{1y}, v_{2y}, v_{3y} \to 0 \text{ as } y \to \infty. \qquad (17b)$$

These correspond to conditions of no normal flow at the coastal wall (17a) and uniform flow far offshore (17b), since we assume all other variables to be uniform far offshore as well.

The equations (16) have only parametric time dependence, so they must hold instantaneously at each time. This suggests the numerical method of solution: for given layer depths, upper layer density, and interior geostrophic velocities, (16) with (17) may be solved for the ageostrophic velocities, and new layer depths, geostrophic velocities, and density obtained by time-stepping the evolution equations (2a), (3), and (8) or (9). This process may be repeated indefinitely. We outline the numerical method more fully in Section III.2.d, and give details in Appendix A.

III.2.b Matching conditions

During sustained upwelling, enough fluid from layer 2 may be entrained into the mixed layer that layer 2 vanishes in the upwelling region. In this case the domain will be

subdivided into subdomains with differing numbers of layers. In these subdomains, (16a,b) or (16c) must be solved according to the number of nonvanishing layers. In order to close the problem, the boundary conditions (17) must be supplemented by three matching conditions at the juncture of these subdomains, the point where the interface between the two interior layers meets the base of the mixed layer. In addition, there is an evolution equation for the location of the juncture.

We assume in the following that adjacent to the coast there is a single two-layer subdomain of finite width, offshore of which lies a semi-infinite three-layer subdomain. This assumption is not necessary, but it simplifies the notation, and it holds for all the numerical results reported here.

Let y2(t) denote the location of the juncture of the two subdomains, so that for $0 < y < y_2(t)$, there are two nonvanishing layers, while for $y_2(t) < y < \infty$, there are three nonvanishing layers. Then $y_2(t)$ satisfies,

$$h_2[y_2(t),t] = 0. \tag{18}$$

Differentiating (18) with respect to t, evaluating (8b) at $y = y_2(t)$, and eliminating $h_{2t}(y_2,t)$ yields an evolution equation for $y_2(t)$:

$$dy_2/dt = v_2[y_2(t),t] + w_e[y_2(t),t]/h_{2y}[y_2(t),t]. \tag{19}$$

We assume that the depths of layers 1 and 3 are continuous across the juncture. This assumption should be appropriate initially, when the uppermost interior layer first vanishes, and will remain so if the derived conditions maintain continuity of the solutions.

We require that ageostrophic (that is, cross-interface) momentum in each layer be continuous across the juncture. Since layer depths are continuous, this implies continuity of velocity:

$$[v_1]^+_- = [v_3]^+_- = 0, \quad y = y_2. \tag{20}$$

where for any function ϕ,

$$[\phi]^+_- = \phi^+ - \phi^-, \tag{21a}$$

$$\phi^- = \lim [(y \to y_2, \ y < y_2)\ \phi], \tag{21b}$$

$$\phi^+ = \lim [(y \to y_2, \ y > y_2)\ \phi]. \tag{21c}$$

Because (10) holds at $y = y_2$, (20) represents only one independent condition.

We have assumed that the layer depths are continuous at $y_2(t)$. In order that they remain so, we must have,

$$d[h_1]^+_-/dt = d[h_3]^+_-/dt = 0. \tag{22}$$

Using (8) and (21), (22) becomes,

$$[(h_1v_1)_y]^+_- = [w_e]^+_- + [h_{1y}]^+_- dy_2/dt. \tag{23a}$$

$$[(h_3v_3)_y]^+_- = -[w_e']^+_- + [h_{3y}]^+_- dy_2/dt. \tag{23b}$$

Here $w_e' = w_e$ in the two-layer region, but $w_e' = 0$ in the three-layer region, where layer 3 is not in contact with the

mixed layer. As is the case with (20), only one of (23) is an independent condition, since (10) and (19) hold.

The condition (23) may appear artificial at first sight, but in a simplified form it can be motivated by consideration of the dynamics. If $h_{3y}^{+} = h_{3y}^{-}$, (23b) becomes,

$$(h_3v_3)_y^{+} = (h_3v_3)_y^{-} - w_e^{-}. \tag{23c}$$

This form of the condition may be derived by formulating an equation similar to (16) that is valid for a composite upper layer that includes both the mixed layer and layer 2, and then letting the width of the transition in the composite layer between the mixed layer and layer 2 approach zero. We give the details of this derivation in Appendix A. It may also be argued that since a discontinuity in layer depths at y_2 would necessitate an unphysical infinite geostrophic shear by the thermal wind relation, the only dynamically consistent condition must be exactly that which maintains continuity of the layer depths.

The third condition is a regularity condition. Using (10) and expanding terms, (16b) may be written as,

$$g(\rho_0 f)^{-1}(\rho_3 - \rho_2)[h_2v_{2yy} + 2h_{2y}v_{2y} + h_{2yy}v_2 + (h_1v_1)_{yy}]$$
$$- (f - u_{2y})v_2 + (f - u_{3y})v_3 = 0. \tag{24}$$

A point where $h_2 = 0$ is a singular point of (24), and thus of the coupled set (16), since the coefficient of the highest derivative of v_2 vanishes there. Solution of (16) by power series shows that three regular solutions and one singular

solution exist in the neighborhood of such a point. In order to remove the singular solution, we impose the regularity condition,

$$g(\rho_0 f)^{-1}(\rho_3 - \rho_2)[2h_{2y}v_{2y} + h_{2yy}v_2 + (h_1v_1)_{yy}]$$
$$- (f - u_{2y})v_2 + (f - u_{3y})v_3 = 0. \qquad (25)$$

This may be derived either by power series solution of (16) or by inspection of (24), requiring that v_{2yy} be bounded at $y = y_2$.

The three conditions (20), (23), and (25), applied at any juncture of two- and three-layer subdomains, close the problem for the equations (16), with the boundary conditions (17), when layer 2 vanishes in any portion of the domain.

III.2.c Nondimensionalization

We nondimensionalize the equations by dimensional quantities related to the forcing. In this subsection, primes will denote nondimensional variables. Typical dimensional values will be given in brackets. The basic scales are the friction velocity u_* [1 cm s^{-1}] and the heating Q_* [75 W m^{-2}], in terms of which the forcing may be written,

$$\tau^x = \rho_0 u_*^2 \tau' \ [0.1 \text{ N m}^{-2}], \ Q = Q_* Q'. \qquad (26a)$$

The nondimensional variables and dimensional scales (with $m_0 = 0.5$ (Davis et al., 1981a, 1981b), $\rho_0 = 10^3$ kg m^{-3}, $g = 9.8$ m s^{-2}, $f = 10^{-4}$ s^{-1}, specific heat of water at

constant pressure $c = 4.1 \times 10^3$ J K^{-1} kg^{-1}, and thermal expansibility $\alpha = 1.7 \times 10^{-4}$ K^{-1}) are,

$$x = \lambda_* x',$$

$$\lambda_* = (g(\rho_*/\rho_0)h_*)^{1/2}/f = 2m_0 u_*/f \quad [100 \text{ m}], \tag{26b}$$

$$t = t_* t', \qquad t_* = \lambda_*/V_* \qquad [3300 \text{ s} = 55 \text{ min}], \tag{26c}$$

$$(h_1, h_2, h_3, H) = h_*(h_1', h_2', h_3', H'),$$

$$h_* = 2m_0 u_*^3/(\alpha g Q_*/c\rho) \qquad [33 \text{ m}], \tag{26d}$$

$$(u_1, u_2, u_3) = U_*(u_1', u_2', u_3'),$$

$$U_* = f\lambda_* \qquad [1 \text{ cm s}^{-1}], \tag{26e}$$

$$(v_1, v_2, v_3) = V_*(v_1', v_2', v_3'),$$

$$V_* = u_*^2/fh_* \qquad [3 \text{ cm s}^{-1}], \tag{26f}$$

$$(\rho_3 - \rho_1, \rho_3 - \rho_2, \rho_2 - \rho_1) = \rho_*(\Delta_{31}, \Delta_{32}, \Delta_{21}),$$

$$\rho_* = \lambda_*(\alpha Q_*/c)(f/u_*^2) \qquad [3 \times 10^{-4} \text{ kg m}^{-3}]. \tag{26g}$$

The vertical scale h_* is the Monin-Obukhov length. The ageostrophic velocity scale V_* results from the balance of Coriolis force and vertical stress divergence, and the geostrophic velocity scale U_* from the inertial balance of Coriolis force and acceleration. The time scale t_* is chosen to balance temporal and advective rates of change. The density scale ρ_* is suggested by the balance of local or advective heating and surface heat flux. The horizontal length scale λ_* is the internal deformation radius formed from h_* and ρ_*. Note that the density and horizontal length scales are small. Much larger density differences and horizontal scales O(1 kg m^{-3}, 50 km) characterize the initial

fields before an upwelling event wipes out the pycnocline at the mixed layer base.

III.2.d Outline of numerical method

We outline the numerical method here, giving the details in Appendix B. All variables are nondimensional in this subsection (i.e., primes on nondimensional variables have been dropped).

We prescribe, on a grid of points, the initial distribution of density, layer depths, and geostrophic velocities:

$$\Delta_{21}(y,0) = \Delta_{210};$$

$$h_i(y,0) = h_{i0},\ u_i(y,0) = u_{i0},\ i=1,2,3. \qquad (27)$$

In the cases we consider here, these will all be constant. The constant density difference Δ_{32} between layers 2 and 3 must also be specified. The initial conditions must satisfy the thermal wind relations (15).

We then solve the boundary value problem for the ageostrophic velocities, (16) and (17), by finite difference methods. In nondimensional form, these equations are,

$$(\Delta_{21}h_1^2 v_{1y})_y - h_1(1 - u_{2y})(v_1 - v_2)$$
$$= \tau + (1/2)[h_1(Q + \Delta_{21}w_e)]_y, \qquad (28a)$$

$$\Delta_{32}(h_3 v_3)_{yy} + (1 - u_{2y})v_2 - (1 - u_{3y})v_3 = 0. \qquad (28b)$$

The nondimensional boundary conditions are identical to the dimensional conditions (17).

When (28) have been solved for the velocities v_i, we time-step the evolution equations for the layer depths, upper layer density, and geostrophic velocities along characteristic curves in the respective layers. We then solve the boundary value problem for the v_i with the new depths, density, and velocities. We repeat this process indefinitely. In a region where layer 2 vanishes, the nondimensional form of (16c), which may be read off from (28a) by replacing each subscript 2 with a subscript 3, replaces (28). The nondimensional matching conditions (20) and (23) are identical to the dimensional conditions, while the regularity condition (25) becomes,

$$\Delta_{32}[2h_{2y}v_{2y} + h_{2yy}v_2 + (h_1v_1)_{yy}] - (1 - u_{2y})v_2 + (1 - u_{3y})v_3 = 0. \tag{29}$$

The differential equations for the characteristic curves $\eta_i(t,y)$ in layer i, i=1,2,3, are,

$$d\eta_i/dt = v_i,\ \eta_i(0,\eta_{i0}) = \eta_{i0},\quad i=1,2,3. \tag{30}$$

Along the interior layer characteristic curves, the interior layer momentum equations (2a) satisfy,

$$du_i(y,t)/dt = v_i(y,t),\qquad i = 2,3, \tag{31}$$

so the geostrophic interior velocities may be evaluated without any additional integration as,

$$u_i(\eta_i,t) = u_{i0}(\eta_{i0}) + \eta_i(t,\eta_{i0}) - \eta_{i0},\quad i=2,3. \tag{32}$$

Along the mixed layer characteristic curves, the evolution equations for h_1 and the mixed layer mass deficit (relative to layer 3 density) $h_1\Delta_{31}$ are,

$$dh_1/dt = -v_{1y}h_1 + w_e, \tag{33a}$$

$$d(h_1\Delta_{31})/dt = -v_{1y}h_1\Delta_{31} + Q + (\rho_3 - \rho_I)w_e. \tag{33b}$$

The last term in (33b) is nonzero only if the interior layer fluid being entrained into the mixed layer has a density different from ρ_3.

In the three-layer subdomain, h_3 may be obtained by conservation of potential vorticity as,

$$h_3 = (1 - u_{3y})h_{30}. \tag{34}$$

Then the remaining layer depth, h_2 in the three-layer subdomain or h_3 in the two-layer subdomain, may be evaluated by (7) as the difference of the total depth H and the known layer depths.

Our method differs from that employed by De Szoeke and Richman (1984) in that we integrate the evolution equations for the geostrophic velocities in layers 2 and 3 and then differentiate with respect to y in order to obtain the geostrophic vorticities needed for the solution of (28). De Szoeke and Richman (1984) solved instead for the interior potential vorticity. This fails in our case because the layer 2 potential vorticity becomes very large as h_2 becomes small, and in fact is singular when h_2 vanishes during sustained upwelling. (An exceptional case, which does not

occur with the initial conditions we consider, is that the layer 2 potential vorticity vanishes identically.) An essentially equivalent alternative to our method is to integrate the equations for the interior vorticities themselves.

We note also that in principle u_2 could be calculated from u_3 and h_3 and the thermal wind relation (15b). However, since the vorticity $1 - u_{2y}$ that appears in (28) may become large, it is preferable for numerical reasons to integrate u_2 directly, rather than use the second derivative of h_3 to evaluate the vorticity $1 - u_{2y}$.

III.3 Thermocline upwelling: numerical results and discussion

Far offshore ($y \to \infty$), the boundary conditions (17) may be invoked, and (28) with (10) reduce to a system of three linear algebraic equations with solution,

$$v_1 = -\tau(h_1^{-1} - H^{-1}),\ v_2 = v_3 = \tau/H. \tag{35}$$

This is the classical Ekman layer (Pedlosky, 1979) modified by the no mass flux condition (10). (If, instead of (10), we were to impose

$$h_1v_1 + h_2v_2 + h_3v_3 = -\tau/h_1, \tag{36}$$

we would get,

$$v_1 = -\tau/h_1,\ v_2 = v_3 = 0, \tag{37}$$

the classical Ekman layer.) By virtue of the boundary conditions (17), the mass flux (35) causes transport

divergence in the mixed layer and convergence in the interior, resulting in upwelling of isopycnals near the coast. The horizontal scale over which this upwelling occurs adjusts dynamically according to (28).

The initial conditions for the cases reported on here were,

$$h_{10} = 0.5 \ [17m], \quad h_{20} = 1.0 \ [33 \ m],$$
$$u_{10} = u_{20} = u_{30} = 0, \tag{38}$$

with total depth H = 10 [330 m] and density differences,

Case 1: $\Delta_{21} = 1000 \ [0.3 \ kg \ m^{-3}]$,
$\Delta_{32} = 100 \ [0.03 \ kg \ m^{-3}]$, (39a)

Case 2: $\Delta_{21} = 5000 \ [1.5 \ kg \ m^{-3}]$,
$\Delta_{32} = 500 \ [0.15 \ kg \ m^{-3}]$, (39b)

Case 3: $\Delta_{21} = 10000 \ [3 \ kg \ m^{-3}]$,
$\Delta_{32} = 1000 \ [0.3 \ kg \ m^{-3}]$. (39c)

In all cases, the forcing was constant,

$$\tau = -1 \ [0.1 \ N \ m^{-2}], \ Q = 1 \ [75 \ W \ m^{-2}], \tag{40}$$

and the total depth H = 10 [330 m]. In the following discussion, we focus on Case 1. When dimensional values depend on the density differences, we give only the dimensional values corresponding to Case 1.

Initially, when the layer depths and density differences are independent of y and the geostrophic velocities vanish identically, the system (28) with (17) may be solved

analytically. Let λ_{12} and λ_{23} be the internal deformation radii associated with the two interfaces,

$$\lambda_{12} = [\Delta_{21}h_1h_2/(h_1 + h_2)]^{1/2} = 18 \ [1.8 \text{ km}], \quad (41a)$$

$$\lambda_{23} = [\Delta_{32}h_2h_3/(h_2 + h_3)]^{1/2} = 9.5 \ [0.95 \text{ km}], \quad (41b)$$

where the variables take their initial values (39a). Then the solution of (28) with (17) is

$$v_i = v_{i0}[1 - (\lambda_1 - \lambda_2)^{-1}(\lambda_1 e^{-y/\lambda_2} - \lambda_2 e^{-y/\lambda_1})], \quad i=1,2,3, \quad (42)$$

where

$$v_{i0} = -\tau(h_1^{-1} - H^{-1}) = 1.9 \ \ [5.7 \text{ cm s}^{-1}], \quad (43a)$$

and

$$\lambda_{1,2} = [A \pm (A^2 - B)^{1/2}]^{-1/2} = 9, \ 23 \ \ [0.9, \ 2.3 \text{ km}], \quad (44a)$$

$$A = (\lambda_{12}^{-2} + \lambda_{23}^{-2})/2, \ B = H/(\Delta_{21}\Delta_{32}h_1h_2h_3), \quad (44b)$$

and λ_1 (λ_2) corresponds to the plus (minus) sign in (44a). (It is not hard to show that $A^2 > B > 0$ for nonzero layer depths and density differences.)

The expressions for $\lambda_{1,2}$ do not yield to convenient simplification, so as a characteristic horizontal scale for the initial motion we take instead the deformation radius λ_{12}. Following De Szoeke and Richman (1984), we obtain an estimate of the vertical velocity W in the upwelling zone by balancing the offshore transport with the vertical mass flux in an upwelling zone of width λ_{12}: $W = v_{10}h_{10}/\lambda_{12}$. This yields an estimate for the time t_1 of "surfacing" of the upper interface,

$$t_1 = h_{10}/W = \lambda_{12}/v_{10} = 9.5 \ [8.7 \text{ hr}]. \qquad (45)$$

A similar estimate for the time t_2 of surfacing of the lower interface is,

$$t_2 = t_1 + h_{20}/(\lambda_{12}W/\lambda_{23}) = t_1 + h_{20}\lambda_{23}/v_{10}h_{10}$$
$$= 19.5 \ [17.9 \text{ hr}]. \qquad (46)$$

The main sequence of events during the numerical integration of Case 1 is depicted in Figure III.2, which shows the evolution of Δ_{31} (normalized by Δ_{32}; Fig. III.2a,d,g,j), the layer depths h_1 and h_2 (Fig. III.2b,e,h,k), and the normal-to-shore transport $h_i v_i$, i=1,2,3 (Fig. III.2c,f,i,l). The dashed lines in Figs. III.2a and III.2e indicate the initial conditions $\Delta_{31} = 1100$, $h_1 = 0.5$, $h_2 = 1.0$. By time $t = 8.1$ [7.3 hr], somewhat earlier than the estimate (45), the base of the mixed layer has nearly surfaced at the coastal boundary (Fig. III.2b). Enhanced entrainment driven by the shallowing has decreased Δ_{31} near the boundary. For $y > 60$ [6 km], the transport (Fig. III.2c) is nearly independent of y and accurately given by the modified Ekman balance (35). For $y < 5$ [0.5 km], layer 2 supplies more onshore transport than layer 3, despite being roughly one-eighth as thick. The small density difference between layers 2 and 3 inhibits the near-shore intensification of the surface divergence from penetrating into the deep interior flow.

Shortly after t = 8.1, the mixed layer deepens abruptly adjacent to the boundary. This process occurs essentially as in the two-layer model, where it has previously been analyzed in detail (De Szoeke and Richman, 1984). A front of width $O(u_*/f$ [100 m]) forms in the mixed layer. Offshore of the front, the mixed layer is shallow and has nearly its original density. Inshore it is deep and has nearly the density of layer 2.

By time t = 16.0 [14.4 hr], this front has been advected offshore to $y \tilde{=} 20$ [2 km] (Fig III.2d). A relative minimum in mixed layer depth is associated with the front (Fig. III.2e). Just offshore of the front, there is a transport divergence in the mixed layer that is nearly balanced by convergence in layer 2 (Fig. III.2f). Just inshore of it, mixed layer convergence is nearly balanced by layer 2 divergence. The stratification prevents the divergence from penetrating into layer 3. The main effect of the divergence and convergence around the front is the propagation with the moving front of a deformation in mixed layer depth.

In each layer, the transport is nearly equal on either side of the front (Fig. III.2f). Inshore of the front ($y \sim$ 15 [1.5 km]), the modified Ekman balance holds roughly as it does far offshore ($y \sim$ 80 [8 km]), although the layer depths are not constant locally. This transport drives a divergence adjacent to the coast precisely as it would in the absence of

an offshore front. The divergence brings layer 3 to the surface. At t = 16.0 [14.4 hr], the interface between layers 2 and 3 meets the base of the mixed layer at the coast (Fig. III.2e).

By time t = 21.0 [19.2 hr], slightly later than the estimate (46), the mixed layer has shallowed near the coast. Enhanced entrainment again decreases Δ_{31} (Fig. III.2g,h) and a second front forms. The first front has been advected offshore with negligible change in its shape except a slight deepening of the associated relative minimum in the mixed layer depth. The point y_2, where layer 2 vanishes, has moved offshore to y ~ 5 [0.5 km]. There is a small divergence in the mixed layer just offshore of y_2 that balances the convergence in layer 2, so that the convergence in layer 3 is essentially continuous across $y = y_2$ (Fig. III.2i). This continuity is the result of imposing (23): the entrainment velocity (5) is small just inshore of y_2 because Δ_{31} is O(100) and h_1 is O(1).

By time t = 25.4 [23.3 hr], the second front has formed and been advected offshore to y ~ 5 [0.5 km] (Fig. III.2j). This front forms in an analogous manner to the first front, though the density contrast is smaller. Since the interior is unstratified inshore of $y = y_2$, the depth penetration of the divergence around the second front is not limited (Fig. III.2l). The divergence has a structure that is similar to

that around the offshore front, except that it extends deeper.

The geostrophic (alongshore) velocities in each layer at t = 25.4 are shown in Figure III.3. There are jets at the upwelled fronts at y ~ 5 [0.5 km], y ~ 45 [4.5 km], with maximum velocities of 15, 50 [15, 50 cm s^{-1}] respectively. The asymmetry in mixed layer depth and density gradients across the front results in asymmetry in the jets: the trailing edge is sharper.

The leading edge of the inshore front moves offshore faster than the point y_2. As a result, it overtakes y_2 soon after t = 25.4 [23.3 hr], and convective instability occurs. Fluid originating in layer 3 that has been entrained into layer 1 is advected in the mixed layer over layer 2, causing an unstable density profile. The numerical integration was halted at this point.

The positions of the two fronts versus time are shown in Figure III.4a. The fronts move offshore with velocities that decrease slightly with time. Figures III.4b and III.4c show the positions of the two fronts for Cases 2 and 3, respectively. The three cases are similar, quantitatively as well as qualitatively. The time of upwelling of each interface and the position of each front scale with the initial internal deformation radii: the times and positions for Cases 2 and 3 may be obtained from Case 1 by multiplying

by $5^{1/2}$ and $10^{1/2}$, respectively. The distance between the two fronts is roughly $1.5\lambda_{12}$ or $3\lambda_{23}$ in each case.

Upper layer characteristics for Case 1 are displayed in Figure III.5a. The fronts move along these characteristics with very little change in form. The velocity $v_1(y,t)$ is just the inverse slope of the characteristics in Figure III.5a. The increase in offshore velocity near the coast associated with the upwelling event at t = 8.1 is visible as a decrease in slope of the characteristics. As the front propagates offshore, the spreading of characteristics on its inshore side illustrates the divergence in the mixed layer. The characteristics may be interpreted as the y-components of particle paths. The x-components must be obtained by time-integrating the geostrophic velocities.

The characteristics in layer 2 are shown in Fig III.5b. They bend slightly as the front passes over them and the local divergence momentarily alters the layer 2 velocity near the front. They are drawn toward y_2 with increasing rapidity as they approach y_2. The characteristics in layer 3 are shown in Figure III.5c. They show a nearly uniform convergence toward the coastal boundary.

III.4 Summary

We have formulated analytically a semigeostrophic model for thermocline upwelling at a coastal boundary and solved

the reduced equations numerically. The model combines a two-layer stratified interior with a mixed layer capable of handling strong horizontal gradients. This combination allows the modelling of the process of upwelling and entrainment into the surface layer of deep, dense interior fluid that is initially isolated from the surface layer by an intermediate layer of less-dense fluid.

We employ two principal analytical simplifications: all flow variables are uniform in the alongshore direction, and semigeostrophic dynamics apply. Though these are idealizations, the equations retain the essential dynamics of wind-driven upwelling. The reduction to one horizontal dimension allows the efficient resolution of a wide range of scales (100 m - 25 km) that are crucial to the proper understanding of upwelling dynamics. The semigeostrophic approximation filters out inertio-gravity waves. The resulting equations are numerically stable with no lateral friction, so that the horizontal scales result solely from the dynamics of the model.

We solve the reduced equations numerically. The flow is driven by an alongshore wind stress and surface heating. A modified Ekman balance forces surface layer fluid offshore, causing a surface divergence and upwelling of isopycnals near the coastal boundary. The horizontal scale of this

divergence is allowed to adjust dynamically by careful consideration of the normal-to-shore momentum balance.

The initial deformation of the interfaces occurs on the scale of the local internal deformation radii. When a layer interface surfaces, intense frontogenetic entrainment events occur as in the simple two-layer model (De Szoeke and Richman, 1984). The interior stratification inhibits the depth penetration of the local divergence and convergence around the initial upwelled front as it forms and is advected offshore.

The intermediate layer eventually becomes entrained completely into the surface layer in the upwelling region. We derive matching conditions to join the resulting two-layer subdomain with the three-layer subdomain. (An algorithm for treating outcropping isopycnals in a similar physical situation has been given by Bleck (1978) for a three-dimensional shallow water model with a much coarser grid. In the present paper, the semigeostrophic approximation and the inclusion of a time-dependent mixed layer alter the mathematical problem considerably.)

Sustained upwelling results in a step-like horizontal profile of surface layer density, as the layer interfaces "surface" and are advected offshore. Two simple results follow from examination of the numerical solutions:

(1) The upwelled horizontal profiles of surface layer density scale with the initial internal deformation radii. The upwelling process (in this simple model) rotates the vertical density profile to the horizontal and stretches it by a factor of the order of an initial deformation radius.

(2) There is surface transport divergence around the upwelling fronts of the same magnitude as the divergence in the upwelling zone adjacent to the coastal boundary. (The magnitude is roughly the offshore Ekman transport divided by the local internal deformation radius associated with the mixed layer base.) However, this divergence is associated only with the deformation of the mixed layer base near the moving fronts. Interior stratification inhibits the depth penetration of the local divergence around the offshore front, and upwelling of the deep interior occurs only at the coastal boundary.

The model retains the essential physics of wind-driven thermocline upwelling. However, it has limitations. Any attempt to directly model specific oceanic conditions must take alongshore variability into account. The neglect of inertio-gravity waves forces the instantaneous establishment of the modified Ekman balance far offshore and shortens the upwelling time scales. The inclusion of shear mixing in the entrainment parameterization would lead to reduced velocities in the geostrophic jets.

Finally, we note that the surface layer divergence may be forced by a wind stress curl rather than the presence of a coastal boundary without altering the essential dynamics of the process. Thus, with suitable rescaling and inclusion of the β-effect, a version of this model may be applicable to the study of wind-driven thermocline upwelling in the great subarctic gyres of the open ocean.

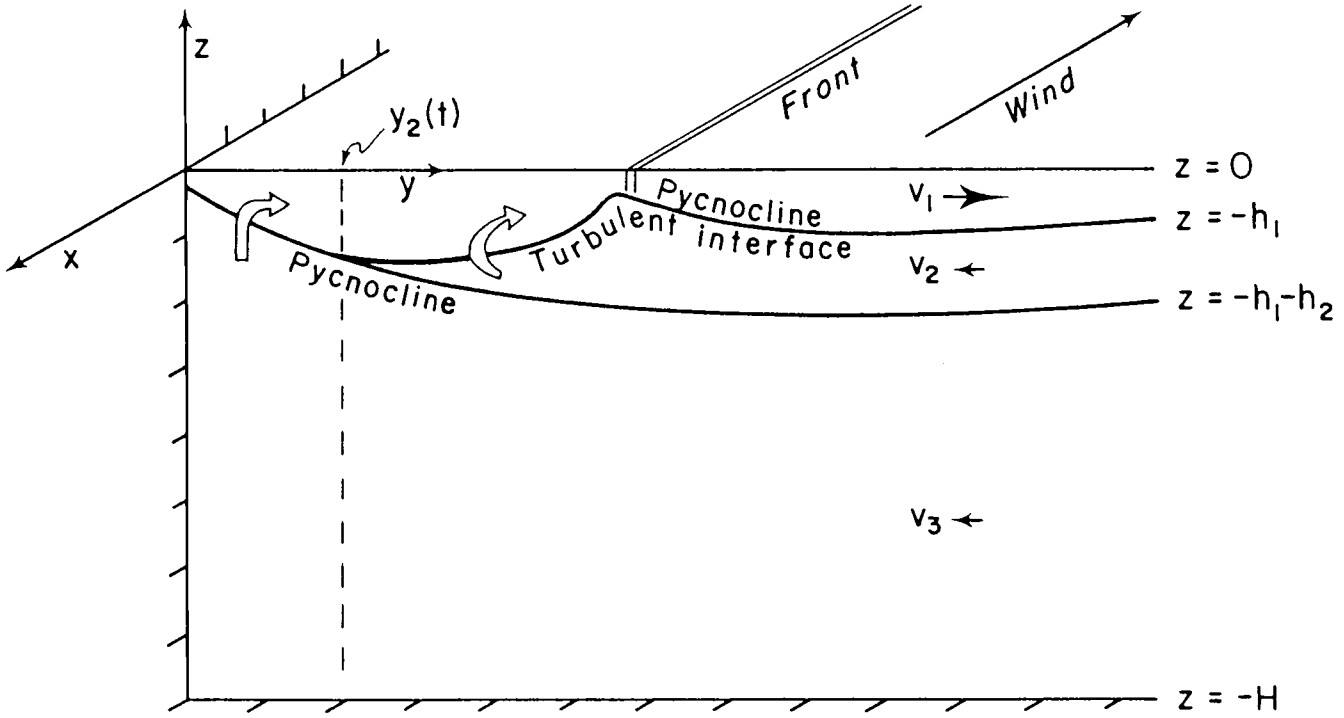

Figure III.1 Model geometry.

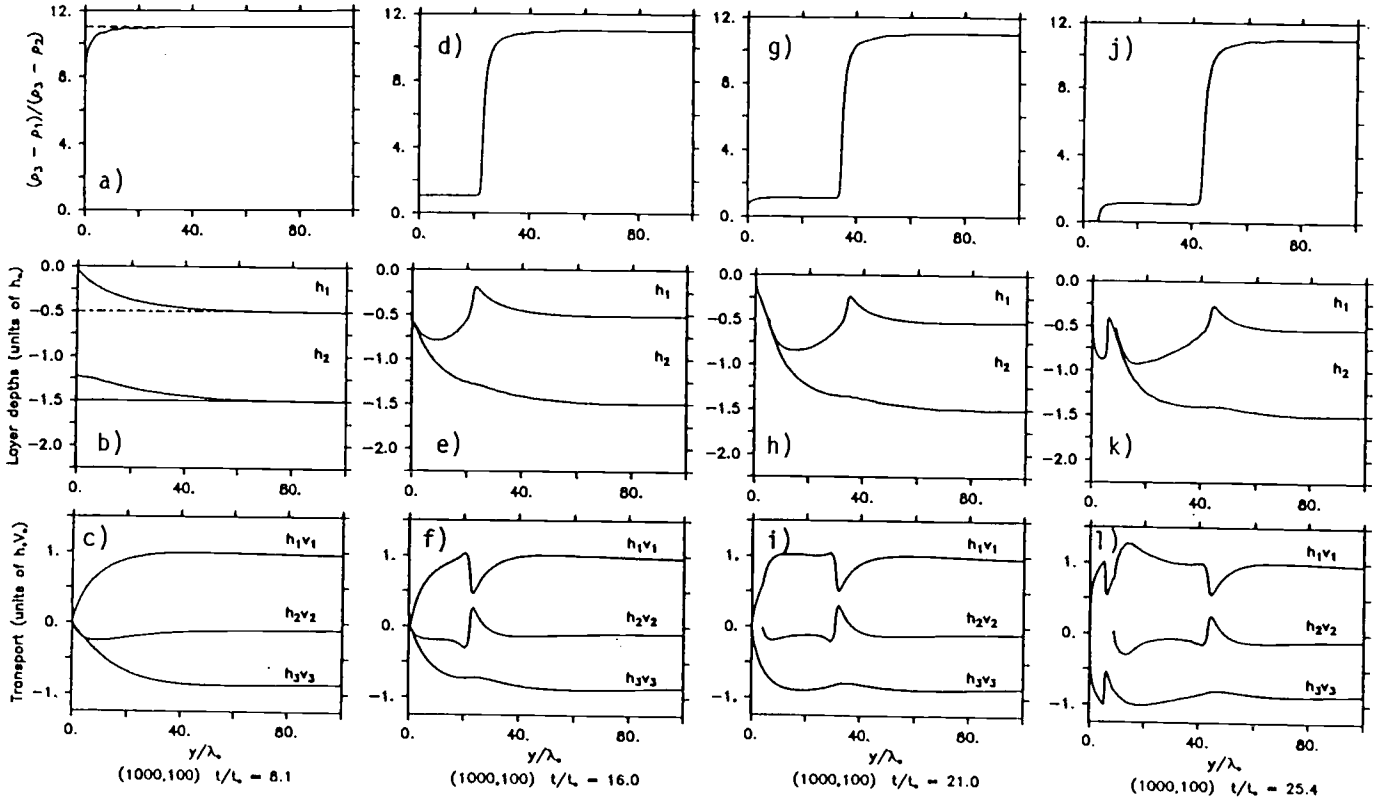

Figure III.2 Nondimensional mixed layer density, layer depths, and normal-to-shore transport vs. offshore distance at times $t/t_* = 8.1$ (a-c), 16.0 (d-f), 21.0 (g-i), 25.4 (j-l). Typical dimensional scales are given by (26).

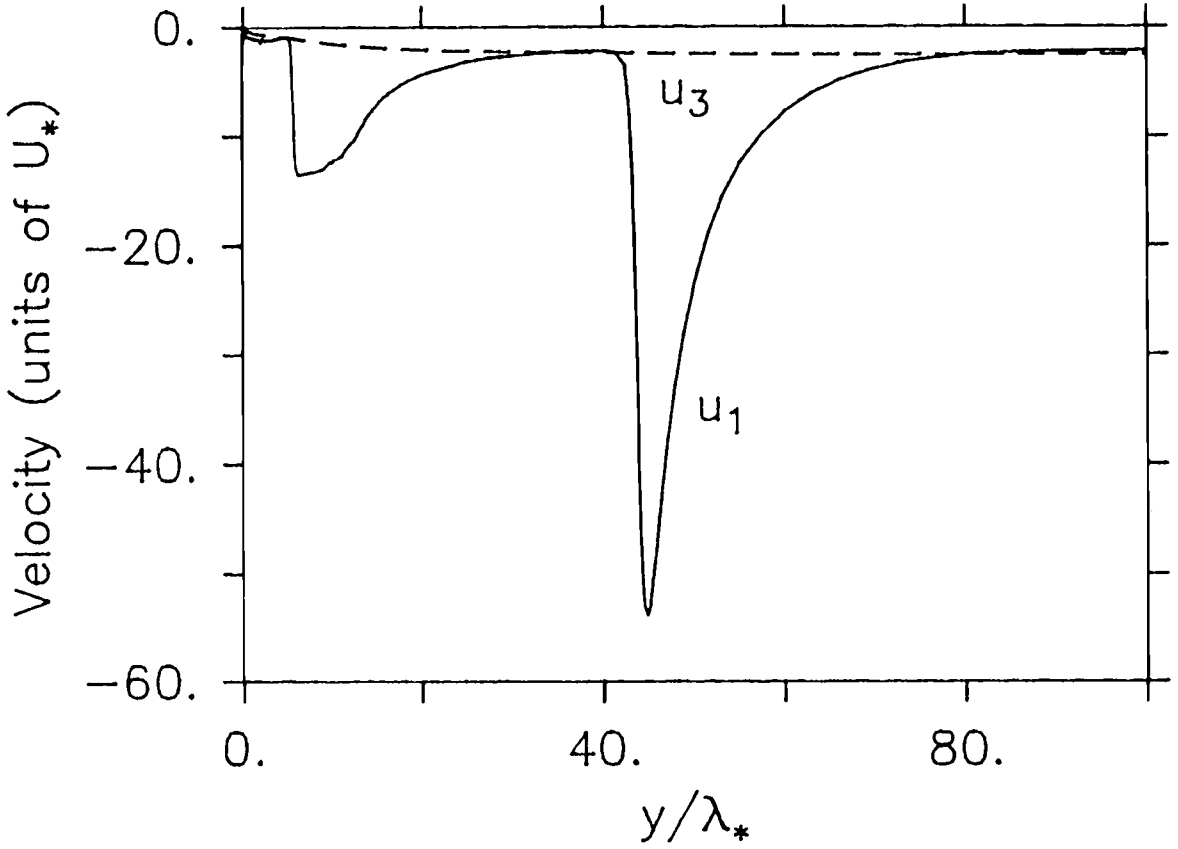

Figure III.3 Nondimensional alongshore geostrophic velocities at time $t/t_* = 25.4$.

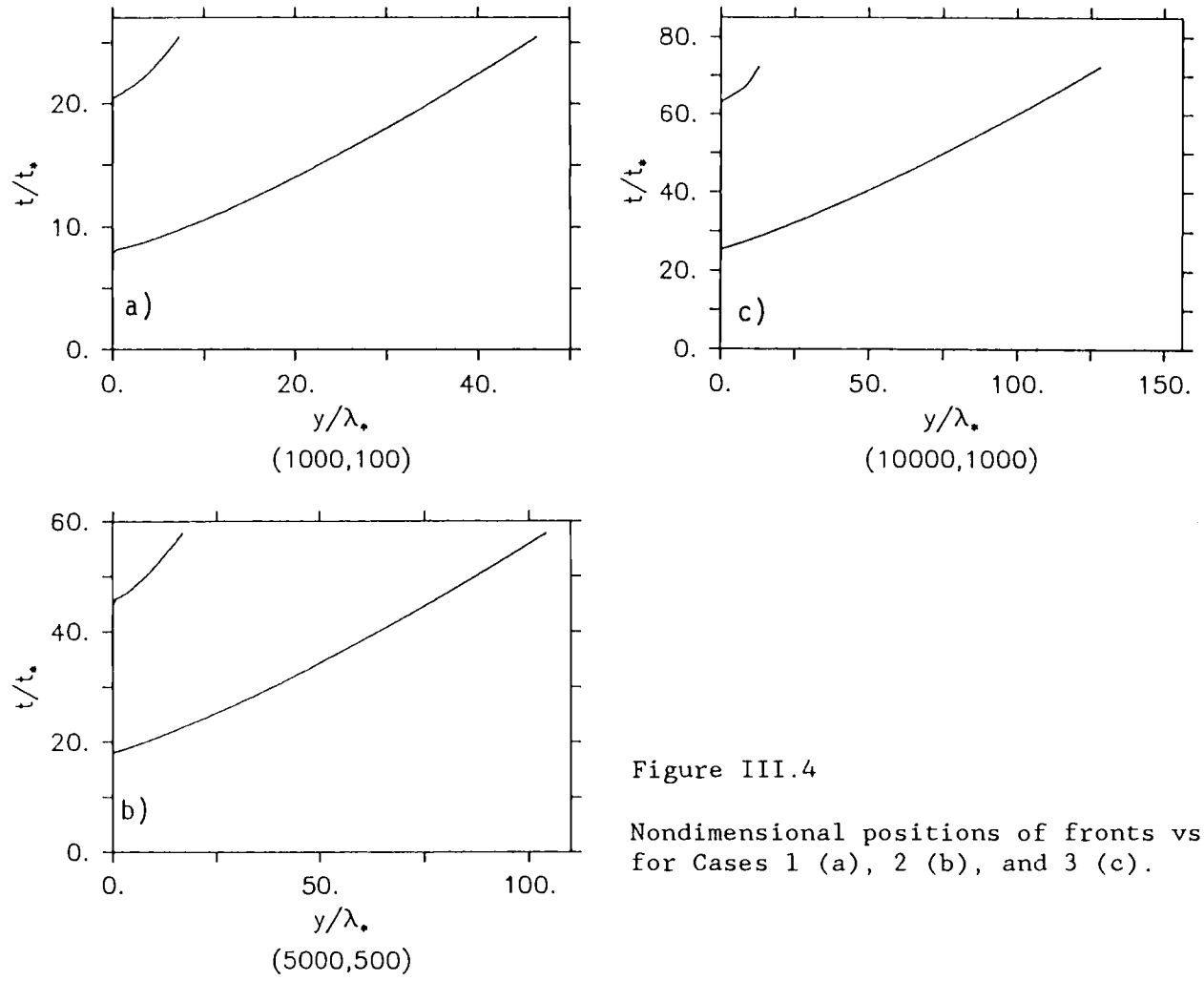

Figure III.4

Nondimensional positions of fronts vs. time for Cases 1 (a), 2 (b), and 3 (c).

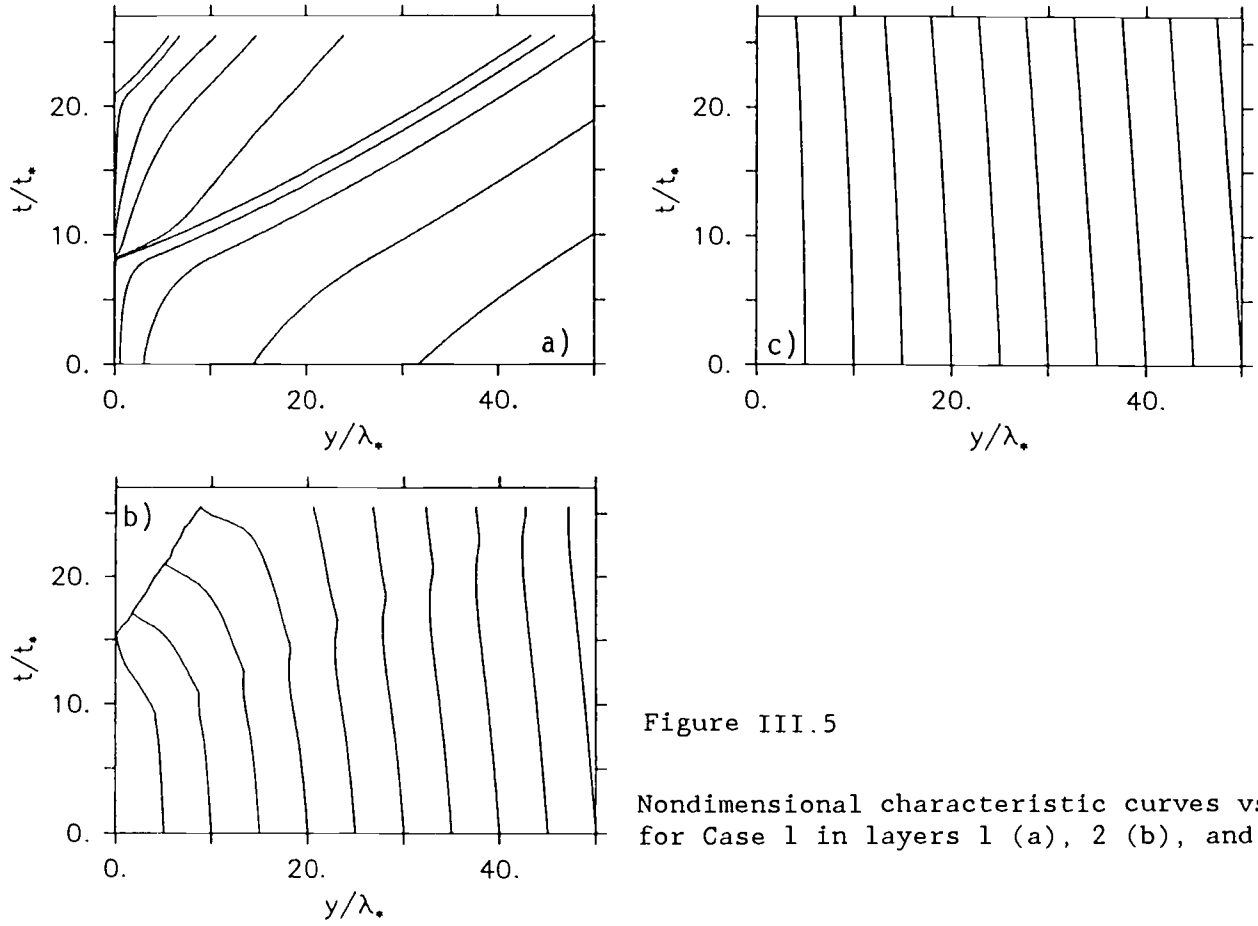

Figure III.5

Nondimensional characteristic curves vs. time for Case 1 in layers 1 (a), 2 (b), and 3 (c).

III.5 References

Bleck, R., 1978: Simulation of Coastal Upwelling Frontogenesis With an Isopycnic Coordinate Model, J. Geophys. Res., 83:6163-6172

Davis, R. E., R. de Szoeke, D. Halpern, and P. Niiler, 1981a: Variability in the upper ocean during MILE. Part I: The heat and momentum balances. Deep Sea Res., 28:1427-1451

Davis, R. E., R. de Szoeke, and P. Niiler, 1981b: Variability in the upper ocean during MILE. Part II: Modeling the mixed layer response. Deep Sea Res., 28:1453-1475

de Szoeke, R. A., 1980: On the Effects of Horizontal Variability of Wind Stress on the Dynamics of the Ocean Mixed Layer. J. Phys. Oceanogr.,10:1439-1454

de Szoeke, R. A., and J. G. Richman, 1984: On Wind-Driven Mixed Layers with Strong Horizontal Gradients -- A Theory with Application to Coastal Upwelling. J. Phys. Oceanogr., 14:364-377

Hoskins, B. J., and F. P. Bretherton, 1972: Atmospheric frontogenesis models: mathematical formulation and solution. J. Atmos. Sci., 29:11-37

Hoskins, B. J., 1975: The geostrophic momentum approximation and the semigeostrophic equations. J. Atmos. Sci., 32:233-242

Kraus, E. B., and J. S. Turner, 1967: A one-dimensional model of the seasonal thermocline: II The general theory and its consequences. Tellus, 19:98-106

Niiler, P. P., 1975: Deepening of the wind-mixed layer, J. Mar. Res., 33:405-422

Pedlosky, J., 1978: A Nonlinear Model of the Onset of Upwelling. J. Phys. Oceanogr., 8:178-187

Pedlosky, J., 1979: Geophysical Fluid Dynamics. Springer-Verlag, 624 pp.

BIBLIOGRAPHY

Batchelor, G. K., 1959: Small-scale variation of convected quantities like temperature in a turbulent fluid, part 1. J. Fluid Mechanics, 5:113-139

Bleck, R., 1978: Simulation of Coastal Upwelling Frontogenesis With an Isopycnic Coordinate Model, J. Geophys. Res., 83:6163-6172

Charney, J. G., 1971: Geostrophic Turbulence, J. Atmos. Sci., 28:1087-1095

Davis, R. E., R. de Szoeke, D. Halpern, and P. Niiler, 1981a: Variability in the upper ocean during MILE. Part I: The heat and momentum balances. Deep Sea Res., 28:1427-1451

Davis, R. E., R. de Szoeke, and P. Niiler, 1981b: Variability in the upper ocean during MILE. Part II: Modeling the mixed layer response. Deep Sea Res., 28:1453-1475

Desaubies, Y. J. F., 1976. Analytical Representation of Internal Wave Spectra, J. Phys. Oceanogr., 6:976-981

de Szoeke, R. A., 1980: On the Effects of Horizontal Variability of Wind Stress on the Dynamics of the Ocean Mixed Layer. J. Phys. Oceanogr.,10:1439-1454

de Szoeke, R. A., and J. G. Richman, 1984: On Wind-Driven Mixed Layers with Strong Horizontal Gradients -- A Theory with Application to Coastal Upwelling. J. Phys. Oceanogr., 14:364-377

Fedorov, K. N., 1986: The Physical Nature and Structure of Oceanic Fronts. Springer-Verlag, 333 pp. (Russian original, Gidrometeoizdat, 1983.)

Garrett, C. and W. Munk, 1972: Space-Time Scales of Internal Waves, Geophys. Fluid Dyn., 2:225-264

Hoskins, B. J., and F. P. Bretherton, 1972: Atmospheric frontogenesis models: mathematical formulation and solution. J. Atmos. Sci., 29:11-37

Hoskins, B. J., 1975: The geostrophic momentum approximation and the semigeostrophic equations. J. Atmos. Sci., 32:233-242

Katz, E. J. and M. G. Briscoe, 1979: Vertical Coherence of the Internal Wave Field from Towed Sensors, J. Phys. Oceanogr., 9:518-530

Kraichnan, R. H., 1967: Inertial Ranges in Two-Dimensional Turbulence, Phys. Fluids, 10:1417-1423

Kraus, E. B., and J. S. Turner, 1967: A one-dimensional model of the seasonal thermocline: II The general theory and its consequences. Tellus, 19:98-106

Kunze, E. and T. B. Sanford, 1984: Observations of Near-Inertial Waves in a Front, J. Phys. Oceanogr., 14:566-581

Large, W. G., J. C. McWilliams, and P. P. Niiler, 1986: Upper Ocean Thermal Response to Strong Autumnal Forcing of the Northeast Pacific, J. Phys. Oceanogr., 16:1524-1550

Lativ, M., 1987: Tropical Ocean Circulation Experiments, J. Phys. Oceanogr., 17:246-263

Leith, C. E., 1971: Atmospheric Predictability and Two-Dimensional Turbulence, J. Atmos. Sci., 28:145-161

McWilliams, J. C. and J. H. S. Chow, 1981: Equilibrium Geostrophic Turbulence I: A Reference Solution in a Beta-Plane Channel, J. Phys. Oceanogr., 11:921-949

Monin, A. S. and A. M. Yaglom, 1975: Statistical Fluid Mechanics, Vol. 2, MIT Press, Cambridge

Niiler, P. P., 1975: Deepening of the wind-mixed layer, J. Mar. Res., 33:405-422

Niiler, P. P., and R. W. Reynolds, 1984: The Three-Dimensional Circulation near the Eastern North Pacific Subtropical Front, J. Phys. Oceanogr., 14:217-230

Paulson, C. A., R. J. Baumann, L. M. deWitt, T. J. Spoering, and J. D. Wagner, 1980: Towed Thermistor Chain Observations in FRONTS 80, Oregon State University School of Oceanography Data Report 85, Reference 80-18.

Pedlosky, J., 1978: A Nonlinear Model of the Onset of Upwelling. J. Phys. Oceanogr., 8:178-187

Pedlosky, J., 1979: Geophysical Fluid Dynamics. Springer-Verlag, 624 pp.

Rhines, P. B., 1979: Geostrophic Turbulence, Ann. Rev. Fluid. Mech., 11:401-441

Robinson, M. K., 1976: Atlas of North Pacific Ocean Monthly Mean Temperatures and Mean Salinities of the Surface Layer, Naval Oceanographic Office Reference Publication 2.

Roden, G. I., 1973: Thermohaline Structure, Fronts, and Sea-Air Exchange of the Trade Wind Region east of Hawaii, J. Phys. Oceanogr., 4:168-182

Roden, G. I., 1975: On North Pacific Temperature, Salinity, Sound Velocity and Density Fronts and their Relation to the Wind and Energy Flux Fields, J. Phys. Oceanogr., 5:557-571

Roden, G. I., 1981: Mesoscale Thermohaline, Sound Velocity and Baroclinic Flow Structure of the Pacific Subtropical Front During the Winter of 1980, J. Phys. Oceanogr., 11:658-675

Van Woert, M., 1981: Satellite Observations in FRONTS 80, SIO Reference No. 81-38.

Van Woert, M., 1982: The Subtropical Front: Satellite Observations During FRONTS 80, J. Geophys. Res., 87C:9523-9536

APPENDICES

APPENDIX A: DYNAMICAL DERIVATION OF A MATCHING CONDITION

The matching condition (23) was derived kinematically in section III.2.b by requiring that the motion maintain continuity of the layer depths at the juncture $y_2(t)$ of the two- and three-layer subdomains. Here we derive it dynamically, in the simplified form (23c), by formulating an equation similar to (16) that is valid for a continuously stratified composite upper layer. Then we may consistently estimate effects due to the discontinuous change at the interface between the two layers by passing to the limit as the upper and lower parts of the composite layer approach layers 1 and 2 of the model.

Consider the schematic geometry of Figure III.1. Near $y = y_2$, the density of layers 1 and 2 will be nearly equal, since layer 1 is composed in that region almost entirely of water that has been entrained from layer 2 and surface heating has little effect on the upwelling time scale. Consider a composite upper layer constructed to contain both layer 1 and layer 2. If the composite upper layer were entirely homogeneous, one might expect the divergence of ageostrophic mass transport in each layer to be continuous at $y = y_2$ (as it should be elsewhere, since the layer depths and velocities are smooth elsewhere). The condition derived below describes how that divergence is modified slightly by the departure of the composite layer from homogeneity. For the

continuously stratified case (with distributions of stress divergence and heating constrained to match those of the original layer 1), the equations analogous to (1) and (3) are,

$$u_t + vu_y + wu_z - fv = (\tau^x(z) - \tau_e(z))/h_1, \tag{A1}$$

$$fu = - p_y/\rho_0, \tag{A2}$$

$$p_z = -g\rho, \tag{A3}$$

$$v_y + w_z = 0, \tag{A4}$$

$$\rho_t + v\rho_y + w\rho_z = [-\alpha Q(z)/c + (\rho_I - \rho_1)w_e(z)]/h_1. \tag{A5}$$

Here u, v, w, p, and ρ are functions of y, z, and t. The advective terms wu_z and $w\rho_z$ must be retained because of the vertical dependence of u and ρ. Layer 3 still obeys the equations (2) with i = 3. For reference, we note the identities,

$$(\phi_B)_y = (\phi_y)_B - \phi_{zB}h_y, \quad (\phi_B)_t = (\phi_t)_B - \phi_{zB}h_t, \tag{A6}$$

where ϕ is any dependent variable in the composite layer, $h = h_1 + h_2$ is the depth of the composite layer, and subscript B means evaluation at z = -h(y,t), the base of the composite layer.

Integrating the hydrostatic equation (2c) vertically gives,

$$p_3 = p_B - g\rho_3(z + h). \tag{A7}$$

Then the use of (20) yields the thermal wind relation,

$$\rho_0 f(u_B - u_3) = - [(p_y)_B - p_{3y}] = - g(\rho 3 - \rho_B)h_y. \tag{A8}$$

In a manner exactly analogous to that leading to (16), making careful use of (A6), an equation for the ageostrophic velocities may be obtained:

$$g(\rho_0 f)^{-1}(\rho_3 - \rho_B)[(h_3 v_3)_{yy} - v_B h_{3yy}] + (f - u_{3y})(v_B - v_3)$$
$$= -(\rho_0 h_1)^{-1}\{\tau^x(z) - \tau_e(z) - [-Q + (\rho_B - \rho_1)w_e(z)]_{hy}\}$$
$$- g(\rho_0 f)^{-1}[(\rho_3 - \rho_B)w_e]_y. \qquad (A9)$$

This may be rewritten as

$$g(\rho_0 f)^{-1}\{(\rho_3 - \rho_B)(h_3 v_3)_{yy} + [(\rho_3 - \rho_B)w_e]_y\}$$
$$= g(\rho_0 f)^{-1}(\rho_3 - \rho_B)v_B h_{3yy} - (f - u_{3y})(v_B - v_3)$$
$$- (\rho_0 h_1)^{-1}\{\tau^x(z) - \tau_e(z)$$
$$- [-Q + (\rho_B - \rho_1)w_e(z)]_{hy}\}. \qquad (A10)$$

Then (A10) may be integrated across the interval $(y_2 - \delta, y_2 + \delta)$, in which the transition layer between the two homogeneous parts of the composite layer meet the surface of layer 3, and the width 2δ of this region allowed to approach zero. If we assume that h_3 is twice differentiable at $y_2(t)$, none of the terms on the right hand side of (A10) will be singular in the limit as $\delta \to 0$, so their integral across this region will vanish in that limit. Since layer 1 consists primarily of fluid that has been entrained from layer 2, the variation in ρ_B is very small. If it is neglected altogether, the left hand side of (A10) may be integrated exactly across the transition region. The result is (23c).

APPENDIX B: NUMERICAL METHOD

The equations solved numerically were (28), (30), and (33), with the boundary conditions (17) and the matching conditions (20),(23), and (29) when appropriate, along with the evaluations (32) and (34). The initial data (27) were given on a grid of 150 points, logarithmically spaced for small y and linearly spaced for large y. Upper layer characteristics were followed continuously, with new points added both adjacent to the boundary and in the interior when divergence in the mixed layer separated grid points. De Szoeke and Richman (1984) successfully integrated the interior layer potential vorticity "backward" (with respect to the interior layer characteristic curves) along the mixed layer characteristic curves. It was necessary to maintain accuracy over longer time scales in the present study, so this approach was abandoned in favor of integrating the interior layer variables along their appropriate characteristic curves. Because grid points moved at different speeds and in different directions along the characteristic curves in the different layers, the values of the interior layer variables were interpolated onto the layer 1 grid for solution of the diagnostic equations (28), and the resulting interior velocities v_2 and v_3 interpolated back onto the interior layer grids for time-stepping. A local quadratic interpolation proved sufficient to maintain

smoothness. The large vorticities that arose in the boundary layer at the coast made spline interpolation impractical. The interior layer grids, which converged toward the coast, were reset regularly, each time the third interior point passed inshore of the second layer 1 point (the first points in each layer were fixed to the coast). The boundary value problem (28) was solved by inverting the five-diagonal matrix finite difference form of (28). Two extra upper diagonals were included to ensure numerical stability in the implementation of the regularity condition (29) at the juncture of the two- and three-layer subdomains.

We were unable to obtain a stable numerical estimate of dy_2/dt for integration of the evolution equation (19) for the location of the juncture between the two- and three-layer subdomains. This was apparently due to the effect of numerical noise, which became appreciable near the point y_2 because of the small layer depths h_2. Consequently, the location y_2 had to be determined implicitly at each time. This was achieved in two steps. First, h_2 was required to vanish on any layer 2 characteristic curve on which it had vanished at any previous time. Second, because by (11) and (13) the layer 3 potential vorticity P_3 was never less than the value it retained as long as layer 3 remained isolated from the mixed layer, the layer depth h_3 calculated from the known geostrophic vorticity and conservation of potential

vorticity was always greater than or equal to the actual layer depth h_3. Thus, h_3 could be calculated everywhere from conservation of potential vorticity, and then replaced with $H - h_1$ in that region where the initial estimate yielded $h_1 + h_3 > H$. The point y_2 was taken to be the farthest offshore point where this replacement was made. It proved useful to place a lower bound of 10^{-3} on nonzero values of h_2 and to require $|v_2| < 5$ where $h_2 < 10^{-2}$. This has no significant dynamical effects but substantially improves numerical stability.

A fourth-order Runge-Kutta time-stepping scheme was used. Convergence was tested by halving the time step on a subset of the numerical integrations. Computations were carried out on the Cray 1A at NCAR. Much of the code was vectorized. A typical integration required several minutes of CPU time.